Fakultät für Physik und Astronomie

Ruprecht-Karls-Universität Heidelberg

Fast dynamic radiography at a high-flux thermal neutron beam

Schnelle dynamische Radiographie an einem thermischen Hochfluss-Neutronenstrahl

Die Diplomarbeit wurde von
Arnd E. Gildemeister
ausgeführt am
PHYSIKALISCHEN INSTITUT HEIDELBERG
unter der Betreuung von
Herrn Privatdozent Dr. Hartmut Abele.

Fast dynamic radiography at a high-flux thermal neutron beam

We report on first dynamic radiographies with millisecond time resolution measured at the new neutron radiography and tomography facility *Neutrograph* at the Institut Laue-Langevin (ILL) in Grenoble (France). We visualized the fuel jet from a diesel direct injection nozzle and recorded dynamic radiographies of a running combustion engine and an externally driven car engine. Further measurements included two-phase flow of pentane in a thin heated steel pipe, water penetration in building materials, and water transport into a lecithin lamellar phase. We put *Neutrograph* into operation at the ILL beamline H9. It provides the high thermal flux of 2.9×10^9 n cm^{-2} s^{-1} and the sufficiently low divergence of 6 mrad that permit fast dynamic radiography with sub-millimeter resolution. The properties of *Neutrograph* are discussed, especially those of the detector.

Schnelle dynamische Radiographie an einem thermischen Hochfluss-Neutronenstrahl

Wir berichten über erste dynamische Radiographien mit einer Zeitauflösung im Millisekunden-Bereich, aufgenommen an der neuen Neutronen Radiographie- und Tomographieanlage *Neutrograph* am Institut Laue-Langevin (ILL) in Grenoble (Frankreich). Wir konnten den Sprüstoß einer Diesel-Direkteinspritzdüse sichtbar machen und haben dynamische Radiographien eines laufenden Verbrennungsmotors und eines geschleppten Automotors aufgenommen. Weiterhin haben wir unter anderem die Zweiphasenströmung von Pentan in einem dünnen erhitzten Stahlröhrchen, das Eindringen von Wasser in Baumaterialien, sowie den Wassertransport in eine laminare Phase aus Lezithin untersucht. *Neutrograph* haben wir am Strahl H9 des ILL in Betrieb genommen. Dieser bietet den hohen thermischen Fluß von 2.9×10^9 n cm^{-2} s^{-1} und die hinreichend niedrige Divergenz von 6 mrad, die schnelle dynamische Radiographie mit einer sub-Millimeter Auflösung erlauben. Die Eigenschaften von *Neutrograph* und insbesondere des Detektors werden dargestellt.

Contents

Chapter 1

Introduction

We put the new neutron radiography and tomography facility *Neutrograph* into full operation in 2003. It is located at the beamline H9 of the Institut Laue-Langevin's research reactor in Grenoble (France). With its unprecedented thermal flux of 2.9×10^9 n cm^{-2} s^{-1} at the moderate divergence of 6 mrad ($L/D \approx$ 150) it opens a wide range of new opportunities in neutron radiography.

The high flux allows the study of dynamic processes in the millisecond range and even below if stroboscopic methods can be used. Applications include the visualization of the gasoline distribution inside combustion engines, two-phase flow in fuel cells, and water transport.

Neutron radiography measures the attenuation of a neutron beam due to absorption and scattering in the sample. It yields information on the nuclear composition of the sample and in this respect it differs greatly from the more common X-ray radiography, which is sensitive to the atomic composition. This is discussed in Chapter 2.

We record radiographies with a detector that consists mainly of a neutron scintillator and a Charge Coupled Device (CCD) camera. It was optimized to fully exploit the high flux. The properties of the beam and the detector are discussed in Chapter 3.

Chapter 4 provides a detailed error analysis. Principal sources of systematic errors are the degradation of the scintillators in the high flux, which can reduce the brightness by up to 28% within 90 min, and systematic beam intensity fluctuations of up to 1.5% in the range of seconds. Statistical errors are essentially determined by the number of neutrons used for a measurement and can be lower than 0.1%. The spatial resolution is typically between 0.2 mm and 0.6 mm. Time resolution depends on the type of experiment; it can be as low as 100 μs.

Our measurements focussed on the visualization of fuel inside combustion engines. The fuel jet of an injection nozzle could be visualized. Dynamic radiographies of a running model-sized combustion engine were recorded but vibrations so far prevented the visualization of the fuel. First measurements with a car engine were done. We also did measurements together with a growing number of external users. These included two-phase flow in a small steel tube, water penetration in building materials, and water transport into a biochemical sample. Measurements are described in Chapter 5.

Chapter 2

Basics of Neutron Radiography

2.1 Measuring Principle

Neutron radiography images samples by measuring their attenuation of a neutron beam with a two-dimensional position-sensitive detector that determines the transmitted neutron flux in a plane perpendicular to the beam.

As neutrons carry no electrical charge they interact predominantly with the nuclei as they pass through matter. The short-ranged strong interaction leads to both absorption and scattering of the neutrons. Electromagnetic interaction with the neutron's magnetic moment only plays a minor role in radiography. The beam attenuation at a given position in the image is described well by

$$I = I_0 \ e^{-\mu \Delta x} \qquad (2.1)$$

where I_0 and I are the incident and transmitted beam intensities, Δx is the thickness of the sample and μ is the attenuation coefficient, a material property that will be discussed in more detail below. For samples consisting of more than one material μ will be a function of space and 2.1 must be rewritten as

$$I = I_0 \ \exp\left(-\int_S \mu(\vec{x}) \mathrm{d}s\right), \qquad (2.2)$$

the path S being a straight line through the sample in the direction of the incident neutrons. We assume a parallel beam geometry; the small divergence limits the spatial resolution (cf. Section 4.4).

One calculates the attenuation from a measurement of I with the sample in the beam and an "open beam" measurement of I_0 without the sample. As the beam is not homogeneous, I_0 is a function of the position in the image.

The attenuation coefficient μ is given by

$$\mu = \sigma_t \frac{\rho N_A}{M} \qquad (2.3)$$

with the material's total cross section σ_t for neutrons, its density ρ, Avogadro's number $N_A = 6.022 \ 10^{23} \mathrm{mol}^{-1}$, and the molar mass M. For samples consisting of several materials this must again be rewritten as

$$\mu(\vec{x}) = \sum_i \sigma_{t,i} \frac{\rho_i(\vec{x}) N_A}{M_i}. \qquad (2.4)$$

The total cross section is

$$\sigma_t = \sigma_s + k_n \sigma_a \qquad (2.5)$$

with the scattering cross section σ_s, the absorption cross section σ_a, and the neutron-energy dependent factor k_n. Scattering occurs both coherently, including Bragg scattering, small angle scattering at grain boundaries, and thermal diffuse scattering for light elements, and incoherently. For neutron wavelengths

greater than the Bragg cutoff the total cross section sharply drops for many materials.

At thermal neutron energies and below, the absorption cross section of most materials shows a reciprocal dependence on the neutron velocity. As absorption cross sections found in tables are usually valid for thermal neutrons with a velocity of $v_0 = 2200$ ms^{-1} the factor

$$k_n = \frac{v_0}{v} \qquad (2.6)$$

has to be used for neutrons with a velocity v [Hug57]. This approximative formula is valid for most materials. A noted exception is the resonance in Gadolinium.

2.2 Tomography

Computer tomography allows a measurement of the attenuation in three dimensions. To do so, radiographies of the sample are recorded under different angles by rotating the sample in the beam. These radiographies are two-dimensional projections of the three-dimensional attenuation of the sample. The inverse Radon transform allows to reconstruct the three-dimensional structure from the projections[Rad17]. Various methods have been developed for the computationally intense reconstruction. Details on computer tomography, its artifacts and limitations have been described elsewhere, e.g. [Kak88]. Specifics on neutron tomography can be found in [Sch99], [Sch01], and [Fer03].

2.3 Comparison with other Methods

Electrons, protons, or X-rays are also used for radiography. The best choice of radiation depends both on the sample and practical considerations. Neutrons are often well-suited for thick samples but their availability is low.

Neutrons penetrate matter more easily than charged particles as the strong force is very short-ranged compared to the long-range Coulomb interaction. While it takes 45 cm of aluminum to attenuate a beam of thermal neutrons to 1% the range of 10 MeV electrons is 2.2 cm [LB90] and that of 10 MeV protons only 630 μm [Bal96].

Photons are also uncharged and X-rays penetrate matter well. Interaction occurs mainly with the atoms' electron shell [Sie55] and the cross sections roughly follow a power law in the nuclear charge Z. This is very different for neutrons, where the cross section depends on the nuclear structure and even two isotopes of the same element may have totally different cross sections (cf. Fig. 2.1).

This means that even thicker layers of metals may be relatively transparent to neutrons while being opaque for X-rays and that neutrons may be sensitive to small differences in nuclear mass where X-rays cannot resolve the difference. For example, neutrons are highly sensitive to hydrogen, which is practically invisible for X-rays. Table 2.1 shows cross sections for the interaction of neutrons with some isotopes.

The major drawback of neutron radiography is the low availability of high flux sources. At the moment only nuclear reactors and spallation sources are capable of producing the flux necessary for dynamic radiography. Portable sources, based on spontaneous fission in ^{252}Cf, cannot usually provide the necessary flux. Care must be used to avoid strong activation of samples through neutron capture, especially for a high flux.
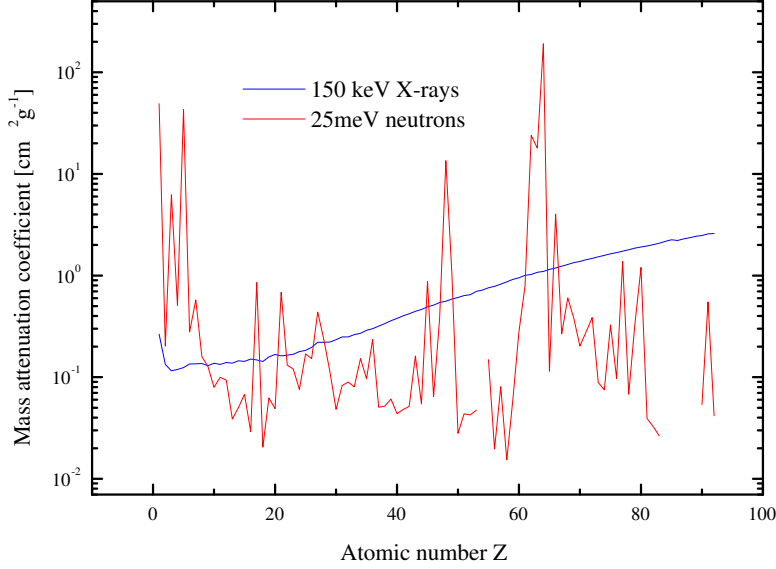
Figure 2.1: Mass attenuation coefficients for neutrons and X-rays. Sources: [Sea92] [Hub96] [IUP01].

Isotope	σ_{s_c} [barn]	σ_{s_i} [barn]	σ_a [barn]
^{1}H	1.76	80.3	0.333
^{2}H	5.59	2.05	5.19×10^{-4}
^{3}He	4.42	1.6	5.33×10^3
^{4}He	1.34	0	0
^{6}Li	0.51	0.46	940
^{7}Li	0.619	0.78	4.54×10^{-2}
B	3.54	1.7	767
^{10}B	0.144	3	3.84×10^3
C	5.55	0.001	3.5×10^{-3}
O	4.23	8×10^{-4}	1.9×10^{-4}
Al	1.50	8.2×10^{-3}	0.231
Fe	11.2	0.4	2.56
Gd	29.3	151	4.97×10^4
^{157}Gd	650	394	2.59×10^5

Table 2.1: Cross sections for coherent (σ_{s_c}) and incoherent (σ_{s_i}) scattering and absorption (σ_a) of thermal neutrons. 1 barn = 10^{-24} cm^2. Where the atomic mass is not specified, data is given for the natural mixture of isotopes. The large cross sections of Gadolinium (Gd) stem from a resonance. Source: [Sea92].

Chapter 3

Beam and Detector

The neutron radiography and tomography facility *Neutrograph* features a high thermal flux of 2.9×10^9 n cm^{-2} s^{-1} [Fer03] and moderate divergence of 6 mrad ($L/D \approx 150$). It is located at the end of a flight tube at a distance of 15.3 m from the source.

After traversing the sample the neutrons hit on a ^{6}Li scintillator where they produce a large number of photons. A mirror reflects the light out of the neutron beam and it is detected by a camera with a Charge Coupled Device (CCD).

Beam and detector allow to study samples of typical sizes of some 10 cm with a spatial resolution of about 0.6 mm and a time resolution of about 1 ms.

A casemate surrounds the sample area to provide shielding against radiation. Newly installed video surveillance cameras, a CO_2 fire-extinguisher, pressurized air, and tubes for radioactive hot exhaust gases allow the study of samples such as combustion engines.
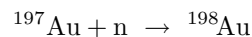
3.1 The Beam

This section deals with three properties of the beam: Its flux or intensity and the temporal stability thereof and its divergence. The former determine measurement times and time resolution, the latter sets a limit on spatial resolution.

The intensity of the beam has earlier been measured to be 2.9×10^9 n cm^{-2} s^{-1} [Fer03]. We have repeated this measurement and, averaged over the central 10×10 cm^2, found the same result. At the brightest spots we found an intensity of up to 3.6×10^9 n cm^{-2} s^{-1}. As during the measurement the reactor was running at 54 MW thermal power instead of the usual 58 MW, this suggests a somewhat higher intensity during normal operation.

We used the standard gold-foil technique to determine the capture flux. Through the reaction

$$^{197}\text{Au} + \text{n} \; \rightarrow \; ^{198}\text{Au}$$

we activated 17 small gold-foils distributed evenly over the beam area during 10 min. Measuring the intensity of the gamma-radiation in the subsequent decay

$$^{198}\text{Au} \; \rightarrow \; ^{198}\text{Hg} + \text{e}^- + \bar{\nu} + 1.4 \text{ MeV}$$
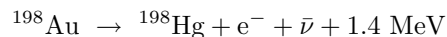
yielded the intensity. The error of such measurements is typically 10%.

Figure 3.1 shows the interpolated intensity distribution of the beam.

For any quantitative measurement it is important to note that this is only the time-average intensity. The intensity fluctuates by up to 1.5%. Figure 3.2 shows the average greylevel of images of the open beam taken every 0.1 s. It is typical and shows that the fluctuations may take place in the range of seconds or below.

These well-known systematic fluctuations are assumed to stem from the movement of the control rod in the fuel element. The beam intensity changes by the
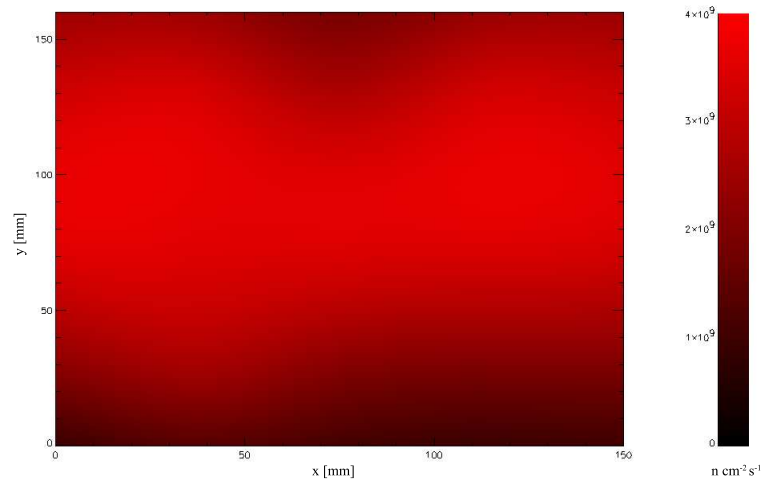
Figure 3.1: The beam as seen by the detector. The intensity was interpolated from gold-foil measurements at 17 points; the error is about 10%. The lower left corner of the plot is at a height of 1303 mm above the floor and at a distance of 877 mm from the left wall. The intensity was measured at a distance of 804 mm from the beam window.
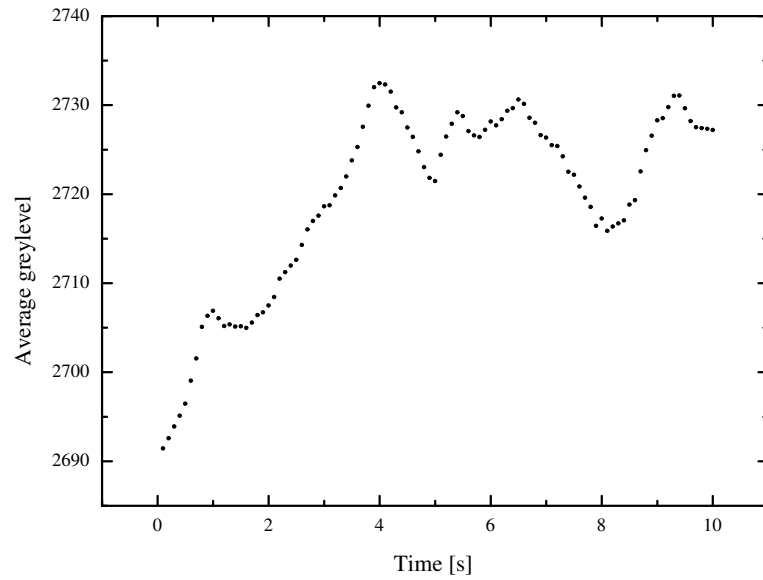

Figure 3.2: Typical fluctuation of the beam intensity. The error due to counting statistics is below 0.1 greylevel.

same order of magnitude over the whole reactor cycle of 50 days as the rod moves out of the fuel element. Intensity changes may even be larger if for technical reasons the reactor power is raised or lowered manually.

Confer to Section 4.1.2 for a detailed discussion of correction mechanisms.

The beam divergence is usually given as the L/D-ratio. $D = 93$ mm is the diameter of the source and $L = 15.3$ m the distance between source and sample, so $L/D = 165$. Earlier measurements with a KOBAYASHI-device [Kob90] yielded an L/D-ratio of 165 ± 36 horizontally and 153 ± 23 vertically [Fer03]. The angle of divergence is given by $\Theta = \arctan \frac{D}{L} \approx \frac{D}{L} = 6$ mrad.

3.2 The Detector

Figure 3.3 shows the principle of detection. Neutrons coming from the object hit on the scintillator screen, where they produce a large number of photons. Mirrors reflect the light out of the neutron beam and a CCD camera detects it. A ^{6}Li dump stops the remainder of the beam.

In the following we will discuss the three main components of the detector, the scintillator, the camera, and the housing that connects them with the mirrors.

3.2.1 The Scintillator

For all experiments reported here we used a ^{6}LiF/ZnS:Cu,Al,Au granular scintillator. An important alternative are glass scintillators.

LiF/ZnS scintillators rely on the large absorption cross section of ^{6}Li. This makes the reaction

$$^6\text{Li} + \text{n} \ \rightarrow \ ^4\text{He} + ^3\text{H} + 4.8 \text{ MeV}$$
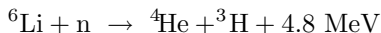
likely even in thin slices of scintillator material. The helium and the triton nuclei lose their kinetic energy in the form of light through collisions with the zinc atoms. Copper, aluminum, and gold shift the wavelength of the emitted light towards green, where the CCD is most efficient. They are available under the trade name NDg from Applied Scintillation Technologies [AST] and were formerly known as NE426. These scintillators have a detection efficiency of about 30% [Czi99] which we could confirm with transmission measurements to an estimated accuracy of 5%. The total number of photons emitted per captured neutron is 1.88×10^5 according to Spowart [Spo69] for similar scintillators. Unfortunately no more recent measurements are available for the NDg scintillator. While Spowart used scintillators of 0.25 mm thickness, the NDg is 0.45 mm thick and the exact composition is not disclosed by the manufacturer. As light emission depends critically on these two parameters, care has to be taken when using the above number. From [Spo69] and our own measurements we estimate that it might easily be a factor of 3 lower. The scintillator's peak emission is at 540 nm (green) [AST00] for the NDg, and the decay to 10% of the maximum intensity within 85 μs [AST00]. Our own measurements with short pulses generated by a neutron chopper confirmed a decay to 10% in under 100 μs but also showed that it may take some 500 μs until all afterglow has ended. The particle size range is $2 - 7$ μm [AST00].

An alternative are ^{6}Li glass scintillators, which have detection efficiencies of about 90% at the cost of a light output of only about 7900 photons per absorbed neutron [Spo69].

Other scintillators use boron or gadolinium for the initial capture reaction and there are also liquid and gas scintillators.

We use LiF/ZnS scintillators because of their high light output, their good spatial resolution, and their ease of use. Drawbacks are the rapid degradation (cf. Section 4.1.1), the relatively low detection efficiency, and the high cost of about 1500 EUR for 20×20 cm^2.
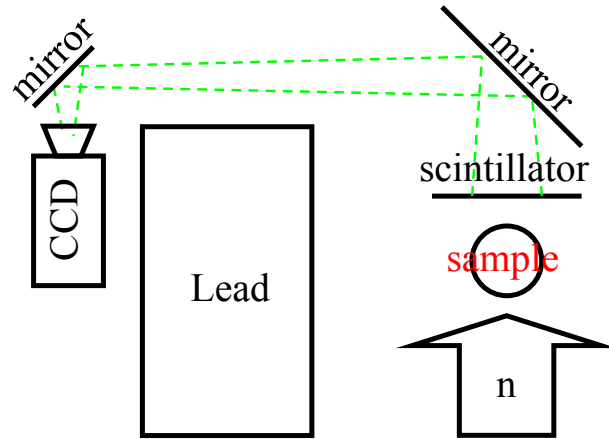
Figure 3.3: Detector setup. After traversing the object the transmitted neutrons arrive on the scintillator screen, where they produce a large number of photons. These are mirrored out of the beam and detected by a CCD camera. Placing the object on a rotational stage allows tomographic acquisitions.
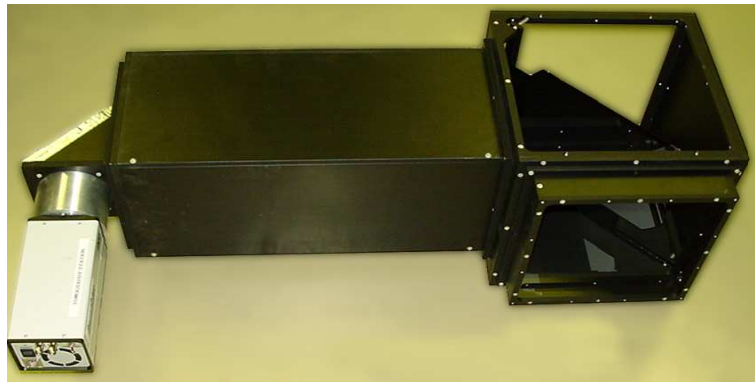

Figure 3.4: Photograph of the detector housing. The CCD camera can be seen on the left. The scintillator was taken off to show the primary mirror.

3.2.2 The Camera

We detect the photons coming from the scintillator with a Charge Coupled Device (CCD) camera.

The availability of affordable CCD cameras gave neutron radiography and tomography fresh impetus. Quick repeatability of the measurements and the immediate availability of the digital data are the obvious advantages over other imaging techniques, such as conventional film, image plates, counting detectors, or video cameras (see e.g. [Sch99]).

CCDs are two-dimensional arrays of light-sensitive areas on a semiconductor. They exploit the ability of photons to create electron-hole pairs in semiconductors through the inner photo effect. In each pixel a MOS (Metal-Oxide-Semiconductor) capacitor creates a potential well that collects these charges. Next to it are more capacitors, so-called phases, that serve two purposes. During exposure they form potential barriers that detach the pixel from its neighbors. After exposure the potentials are changed such that the collected charges are transferred into the first phase but are still separated from the neighbor. Then the charge is moved on to the second phase and eventually to the first phase of the neighbor along a line of a pixels. At the end of the line the charge moves on to an amplifier and finally to an analog to digital converter. This way of reading out the chip is referred to as Interline-Progressive-Scan. Short introductions to CCD technology can be found in [SIT94] or [Ott02].

The amount of charge created on the CCD is linear in the photon flux and the exposure time but only a fraction of the photons create charges. This fraction is called the quantum efficiency.

The principal sources of noise are dark current and readout noise. Thermal motion can always create electron-hole pairs even when the CCD is shielded against light. This dark current can be efficiently suppressed by cooling the CCD and plays no role for the short exposure times typical for our setup. Readout noise occurs each time the CCD is read and is independent of the charge. The signal-to-noise ratio can therefore be improved by collecting as much charge as possible.

For most of the experiments reported here we used a hybrid of the *SensiCam fast shutter* and the *SensiCam long exposure* from the PCO AG [PCO]. It has an Interline-Progressive-Scan CCD with 640×480 pixels with an area of 9.9×9.9 μm^2 each to give a total chip size of 6.3×4.8 mm^2. The quantum efficiency is larger than 40% at 520 nm. A peltier element cools the CCD to $-15°$C, which reduces the dark noise to less than 0.1 e$^-$ s^{-1} pixel^{-1}. The charges are counted with a 12-bit analog-to-digital converter with a factor of 7.5 e$^-$ per greylevel and a readout noise of 13 e$^-$. The possible exposure time ranges from 100 ns to 1000 s and one can read up to 30 full images per second [PCO02]. It offers the possibility of on-chip integration. This means that the CCD is exposed to light and charges are collected at the pixel several times before reading it. In some situations this can improve the signal-to-noise ratio but one has to keep in mind that the CCD is not entirely insensitive to light during non-exposure times.

We used a standard Nikkor lens with f=50 mm and F=1.2 from the Nikon Inc. [Nik].

After switching on the camera it may take well over an hour until it runs stably. Before, the greylevel measured for a constant light source changes over time. The final stability of the camera is not known precisely.

3.2.3 The Detector Housing

The scintillator, two mirrors, and the CCD are held in place by the detector housing. This aluminum box also shields against unwanted light not stemming from the scintillator. Based on our previous experience the author has de-

signed a new housing with the following features.

It is made entirely out of aluminum and the material directly exposed to the neutron beam was kept to a strict minimum. This has the practical advantage that the beam activates only little material and that this activity quickly decays, as the half-life of aluminum is only 2.3 minutes. About 15 minutes after shutting off the beam one can re-enter the casemate, provided that no other sources of radioactivity, such as activated samples, are present. The housing is sufficiently large to exploit the whole beam area and the modular construction is very flexible and makes different optical path lengths possible. Overlapping edges minimize the intrusion of light from the outside and a black anodization of the aluminum reduces the reflection of light inside the housing. Figure 3.5 shows a drawing of the housing.

The primary mirror reflects the light from the scintillator out of the remaining neutron beam and a secondary mirror reflects it towards the camera. The sole purpose of this construction is to make a sufficient shielding of the sensitive CCD camera against neutrons and gamma-radiation possible. We use a shielding of 5 mm B_4C in rubber against neutrons and 200 mm of lead between sample and camera and 50 mm in all other directions against gamma-radiation.

The primary mirror consists of silicon, aluminum, and sapphire. A $270 \times 200 \times 0.750$ mm^3 Si slice, cut from a 300 mm wafer and polished, serves as the mechanical support. Sputtered on this is a 100 nm thick layer of Al, which has a high reflectivity of over 90% for visible light. A layer of 1 nm sapphire (Al_2O_3) protects the Al against oxidization without deteriorating the reflectivity. This special mirror was produced at the ILL. It is very thin and uses only materials with low scattering cross-sections, thereby reducing the scattering of neutrons towards the camera. Mirrors without a protective layer quickly showed signs of oxidization and their reflectivity declined. A protective layer of 5 nm Si significantly reduced the reflectivity and made the mirror yellowish.

As a secondary mirror we use a regular surface mirror because the neutron flux at this position is already very low.

Both mirrors are glued onto their supports to avoid mechanical stresses as they show up when screwing them on. Thereby we prevent bending the mirrors. This is important because even slightly bent mirrors introduce severe imaging artifacts. Unfortunately, organic glue is a strong neutron scatterer.

Obviously, the scintillator has to be in the focal plane of the imaging system. If either of the mirrors is tilted, this plane is no longer aligned with the housing, rendering a precise focussing of the scintillator impossible. To correct this, three screws hold the primary mirror's support and allow to tilt it. This way the scintillator can be brought in focus.

Different optical path lengths can be realized with the housing to adjust the field of view and the distance between scintillator and camera to the experimental needs.

3.3 The Casemate

The casemate is a shielding made of heavy concrete that surrounds the sample and detector and provides radiation protection. We shortly discuss the safety aspects of the casemate.

3.3.1 Radiation Protection

Radiation protection is necessary because next to the sample the dose rate goes up to 0.1 Gyh^{-1} during irradiation.

The casemate walls consist of 1 m of heavy concrete and the roof is made out of 1 m of regular concrete. The interior is covered by 5 mm of B_4C in rubber to prevent activation by neutrons. During
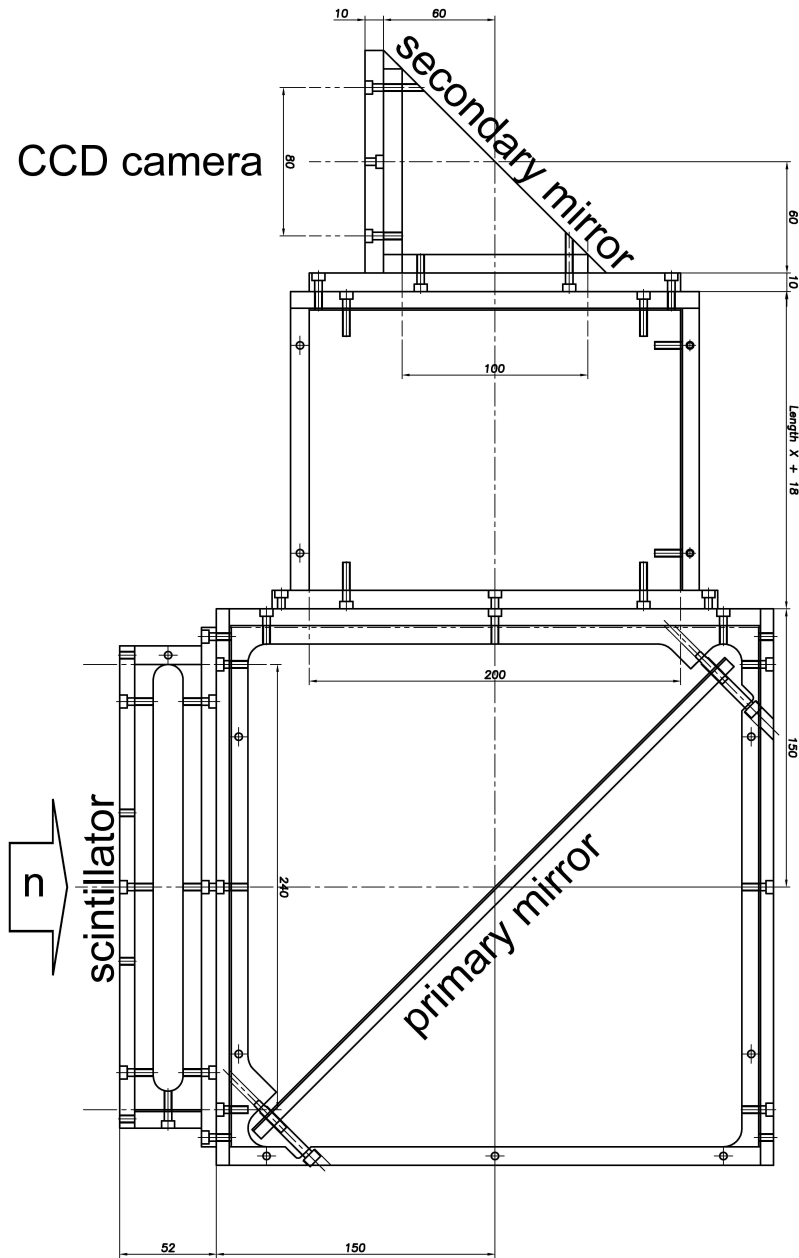
Figure 3.5: Drawing of the detector housing. The primary mirror is at the bottom, the secondary mirror at the top, and the neutrons traverse the primary mirror from left to right. The optical paths are 50 mm in the scintillator box, 300 mm in the primary mirror box, and 140 mm in the secondary mirror box. The connecting box between primary and secondary mirror allows to change the total optical path length. Currently available are boxes with $X = 102$ mm to give a total optical path of 610 mm and with $X = 492$ mm to give a total optical path of 1000 mm. All boxes can be rotated in steps of 90 degrees. The scintillator box is optional.

irradiation a concrete door on rails blocks the entrance. Fig. 3.6 shows a sketch of the casemate.

The main beam shutter consists of 1 m of heavy concrete. It is pneumatically moved out of the beam and closes in case of an alarm. It takes about 25 s to open and during that time neutrons activate the sample while it is not yet possible to start the measurement. We significantly decreased the unnecessary activation of the sample by installing a fast pneumatic shutter in the outer casemate. It consists of 50 mm of borated polyethylene, attenuates thermal neutrons by more than a factor of 100, and opens within 1 s.

3.3.2 Safety

Two newly installed video cameras allow to survey the casemate during irradiations. They help to check the correct operation of the experiment and also increase safety. We chose low-cost cameras without radiation protection that will have to be replaced about once a year.

For the experiments with combustion engines we installed a CO_2 fire-extinguisher. Pulling a lever outside the casemate empties a CO_2-bottle into the casemate. This should efficiently extinguish a fire within a few seconds. We opted against automatic smoke- or heat-detectors to avoid false alarms. This solution obviously requires the careful attention of the experimenter to quickly notice a fire.

For the same experiments we installed a tube connecting the casemate to the reactor's system of radioactive exhaust gases. The system is designed to accept some $10 \ \mathrm{ls}^{-1}$ of gases with a low activity. The first 5 m are made out of metallic tombac tube. With its large surface it efficiently cools down hot gases to almost room temperature. The rest of the tube is made out of plastic. The exhaust gas system must always be below atmospheric pressure. A pressure gauge in the tube closes an electrical contact if the pressure gets too high. We use this to automatically stop the experiment.

Figure 3.6: Sketch of the casemate.

reactor

H9 beam tube
∅ 90 mm

nuclear physics instrument

200×200 mm^2 boron aperture

secondary shutter for thermal neutrons
with apertures of various sizes

inner casemate

main beam shutter at 13 m

fast shutter

sample at 15.3 m

outer casemate
free area: 1.6×2.6 m^2

Neutrograph

reactor wall

Main H-iron

all distances measured from
front end of beam tube

approximate scale
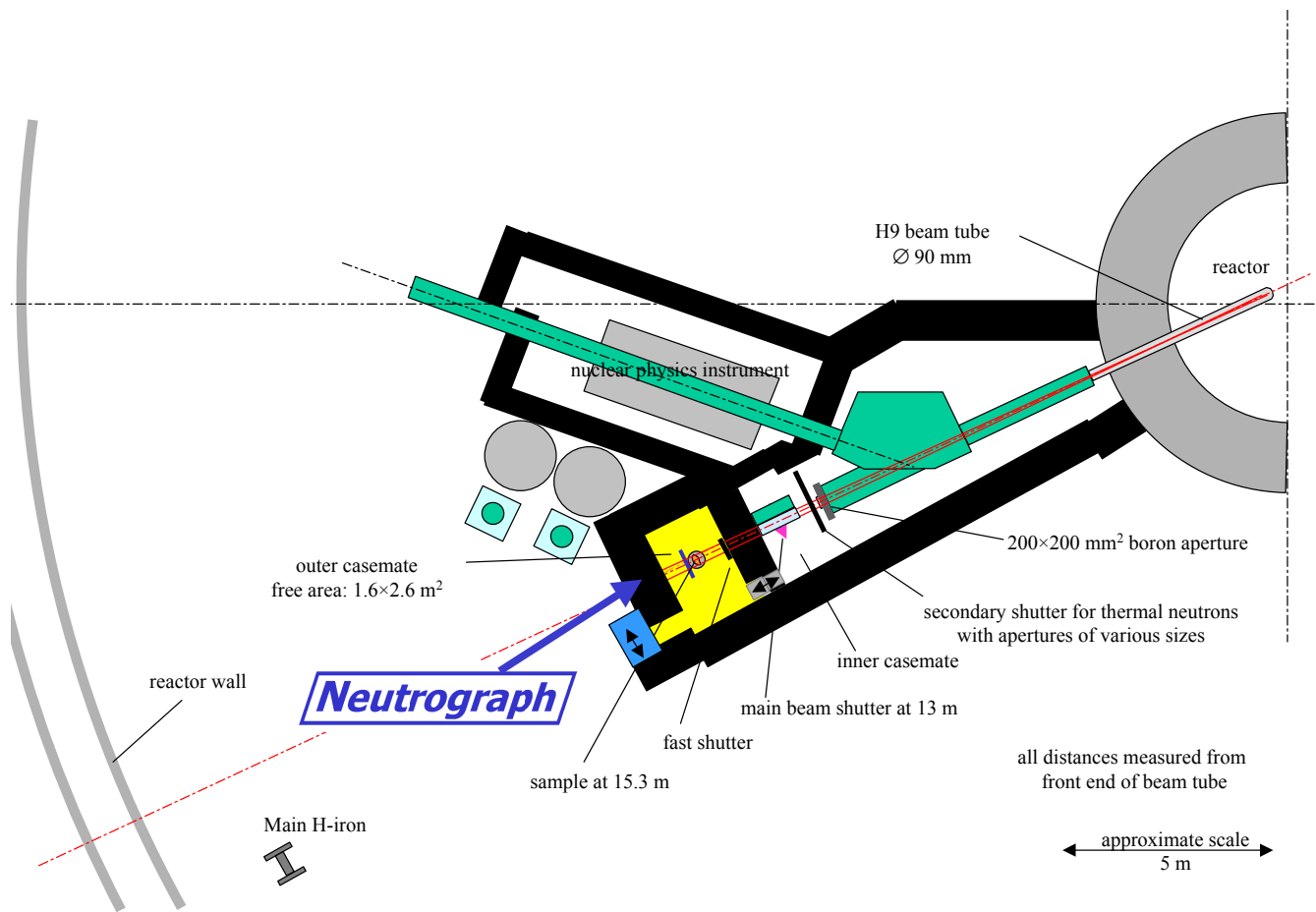5 m

Chapter 4

Error Analysis

The aim of dynamic radiography is to measure the beam attenuation by the sample as accurately and precisely as possible with good spatial and time resolution. The achievable accuracy is limited by statistical and instrumental constraints and depends on the desired accuracy in time and space.

Our measurements regarding combustion engines required an accuracy at the sub-percent level. Therefore, we will discuss errors in some detail.

The main source of statistical errors are statistical fluctuations of the neutron flux. Other known sources of statistical errors are photon noise behind the scintillator and readout noise of the CCD.

Known systematic error sources are temporal fluctuations of the beam intensity and the degradation of the scintillator's light output.

While we can correct for the systematic errors at least in part, the statistics can in most cases only be improved by increasing the exposure time, which often means sacrificing time resolution.

We used the Interactive Data Language (IDL) from Research Systems, Inc. [RSI] to implement the correction mechanisms and data treatment routines described below. It offers versatile and powerful tools for image treatment and is very user-friendly.

The last section of this chapter provides an overview over the different steps in data evaluation.

4.1   Systematic Errors

We found two major sources of systematic errors: the degradation of the scintillator and fluctuations of the beam intensity. For rough, qualitative measurements or very quick measurements one may ignore them. In any experiment aiming at a quantitative result with an accuracy on the percent-level and consisting of several images, they require some consideration.

4.1.1   Scintillator Degradation

During use, the light output of the LiF scintillators (NE426 and NDg) decreases. Experimentally we make the following observations:

- Initially being white or light-green, the scintillator turns brownish in the beam.

- The light-output from a constantly irradiated area decreases roughly exponentially.

- The decrease is slower in areas shielded against neutrons by the sample than in unshielded areas.

These effects were also observed at other neutron radiography experiments such as NEUTRA at the PSI in Switzerland [Leh03] or at the KFKI research reactor in Hungary [Bal03]. Yet, as the neu-
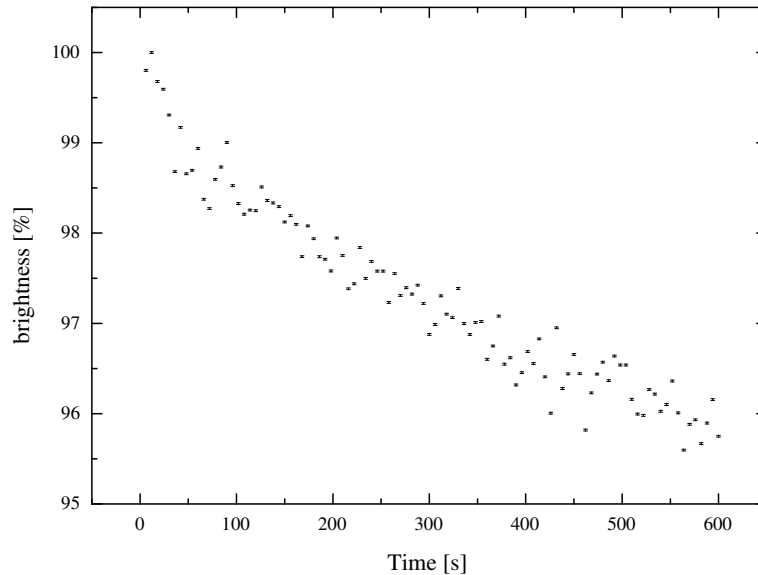
Figure 4.1: Brightness of an NDg scintillator as a function of time. The error bars represent statistical errors due to counting statistics as described in Section 4.2. Two effects can be seen: The quick fluctuations of the beam intensity, which are described in Section 4.1.2, and the much slower degradation of the scintillator.

tron flux is much lower, the effects are also much weaker there.

Figure 4.1 shows the typical behavior of the brightness of a new piece of NDg scintillator over time. With brightness we mean the light output per incoming neutron. Plotted is the brightness averaged over an area of 16 cm^2 on the scintillator. The quick fluctuations are due to systematic changes of the neutron flux and are not due to counting statistics. The slow decrease comes from the scintillator degradation.

If an experiment can be carried out within a few minutes, the decreasing brightness is negligible. For longer experiments aiming at quantitative results it cannot be neglected anymore.

The degradation slows down during irradiations of several hours and shows a roughly exponential behavior with a large offset.

This suggests either a correction mechanism based on a knowledge of the scintillator's behavior or a long irradiation of the scintillator in order to make it stable.

Corrections are difficult. The intensity arriving on the scintillator varies from spot to spot due to different attenuations by the sample and inhomogeneities of the beam. Yet, the degradation depends on the intensity in an unknown way. Moreover, the degradation seems to depend not only on the momentary intensity but also on its history. So far, we only found that, unsurprisingly, the decay

is slower for lower intensities.

No systematic attempt to stabilize the brightness with long irradiations has been made so far. Yet, experience shows that even after irradiations of several hours the brightness decreases.

We assume that the neutrons or secondary particles destroy the organic matrix of the scintillator and thereby change the color. It must be the scintillator's increasing opaqueness to its own light that decreases the brightness and not the depletion of ^{6}Li nuclei.[1] The manufacturer of the NDg scintillator quotes photolysis in ultraviolet light as a factor in the scintillator's degradation [AST00] and of course it is subject to a highly radioactive environment.

We tested two other scintillators: The AST glass scintillator [AST01] and a Gadolinium scintillator prepared by the group of E. Lehmann [Leh03] from the PSI in Switzerland. While the glass scintillator showed a similar degradation as the NDg scintillator, the Gadolinium scintillator showed no signs of a decreasing brightness but has a very much lower brightness to begin with.

To compare the NE426 and the glass scintillator we recorded an image of the open beam with both, shielded half of each with 50 mm of borated polyethylene and 3 mm of Cd against neutrons, irradiated them for 95 min, removed the shielding, and recorded an image of the open beam again. The brightness decreased as follows:

	shielded	unshielded
NE426	$(2 \pm 2)\%$	$(28 \pm 2)\%$
glass	$(3 \pm 2)\%$	$(9 \pm 2)\%$

---

[1] Let's assume a constant incoming neutron flux $I = 3 \times 10^9$ n cm^{-2} s^{-1} and a constant number of photons emitted per captured neutron. Then the light-output is determined by $Q_{sc} \approx n\sigma$, where Q_{sc} is the scintillator's conversion efficiency, n is the area density of ^{6}Li atoms and $\sigma = 940$ b is the cross-section for absorption [Neu02]. As the ^{6}Li-atoms are used up, $\dot{n} = -n\sigma I$, and therefore $Q_{sc} \propto n \propto exp(-\sigma I t)$. The expected time constant $(\sigma I)^{-1} = 4 \times 10^{11}$ s $= 10^8$ h is by far longer than what we observe.

The error range of 2% is a conservative estimate of the possible intensity fluctuations occurring between the measurements. These could not be corrected for in this case. It is possible that the brightness declined even in the areas shielded against neutrons. However, it is also possible that the beam intensity was somewhat lower during the measurement after the irradiation.

We deduct from these measurements that the glass scintillator is about a factor of three more stable than the NE426 or NDg but that its brightness also changes significantly over time. As it produces much less photons than the NE426 (cf. Section 3.2), it is probably not a suitable alternative.

The Gadolinium scintillator consists of a supporting aluminum plate sputtered on which are 5 μm of Gd. The Gd layer is covered by so-called α-foil, a 100 μm thick polyethylene foil with a 40 μm thick layer of ZnS. Conversion electrons from neutron capture by the Gadolinium create light in this foil.

So far, only preliminary tests were done with this scintillator. They showed that even after two hours of irradiation its brightness does not change. Unfortunately the brightness is about 50 times smaller than for the NDg.

Three solutions of the problem are thinkable. In the best case, stable scintillators can be developed. They must have a sufficient brightness in order not to deteriorate the statistics (cf. Section 4.2). Alternatively, a theoretical understanding for existing scintillators could be developed. It would have to be good enough to allow efficient corrections. Finally, the time during which the scintillator is exposed to the beam could be significantly reduced. This might be done with ultrafast shutters or choppers, opening the beam only during the camera's exposure time.

4.1.2   Intensity Fluctuations

The neutron flux coming from the ILL's reactor fluctuates by up to 1.5% on the timescale of minutes or seconds (cf. Section 3.1). In any measurement aiming at a higher accuracy this has to be accounted for.

We correct this effect by normalizing all images of a series to the average greylevel of an area with constant neutron transmission. This assumes that the neutron flux changes equally at all points, which will be justified below.

We position samples such that a part of the field of view has either direct view of the open beam or is only shielded by objects with constant neutron transmission that do not move. In the ideal case of a perfectly constant neutron flux, the average greylevel measured for this area would be constant from image to image. Practically it changes as the beam intensity changes. To correct this, we multiply the greylevels of each image with a factor such that these changes are compensated.

The number of pixels used for this correction has to be chosen in a way that the expected statistical fluctuations on their average greylevel is much smaller than the fluctuations of the beam intensity and the intended accuracy of the measurement (cf. Section 4.2).

This correction mechanism assumes that the changes of the beam intensity are identical throughout the beam's cross section. Therefore we compare the development of the average greylevel of different areas in the same measurement.

Figure 4.2 shows the development of the four quadrants in a series of images. To quantify the behavior in the four quadrants, we calculate the quotients of the average greylevel of the different quadrants as a function of time. Figure 4.3 shows the results. Were the neutron flux changes exactly identical, these quotients would be constant. Instead, they vary on the 10^{-3} level, which gives an estimation of the goodness of the above correction mechanism.

If a decrease of the scintillator's brightness can be expected throughout the measurement, the above procedure must be modified in order not to interfere with other corrections. Rather than choosing the correction factor so that the normalization area always has the same average greylevel, they should be chosen such that it shows the expected decay of the scintillator.

For large samples that fill the entire field of view it would be desirable to have an independent measure of the beam intensity. Tests with a He-detector with relatively low efficiency as well as the signal from an ionization chamber in the reactor pool have started.
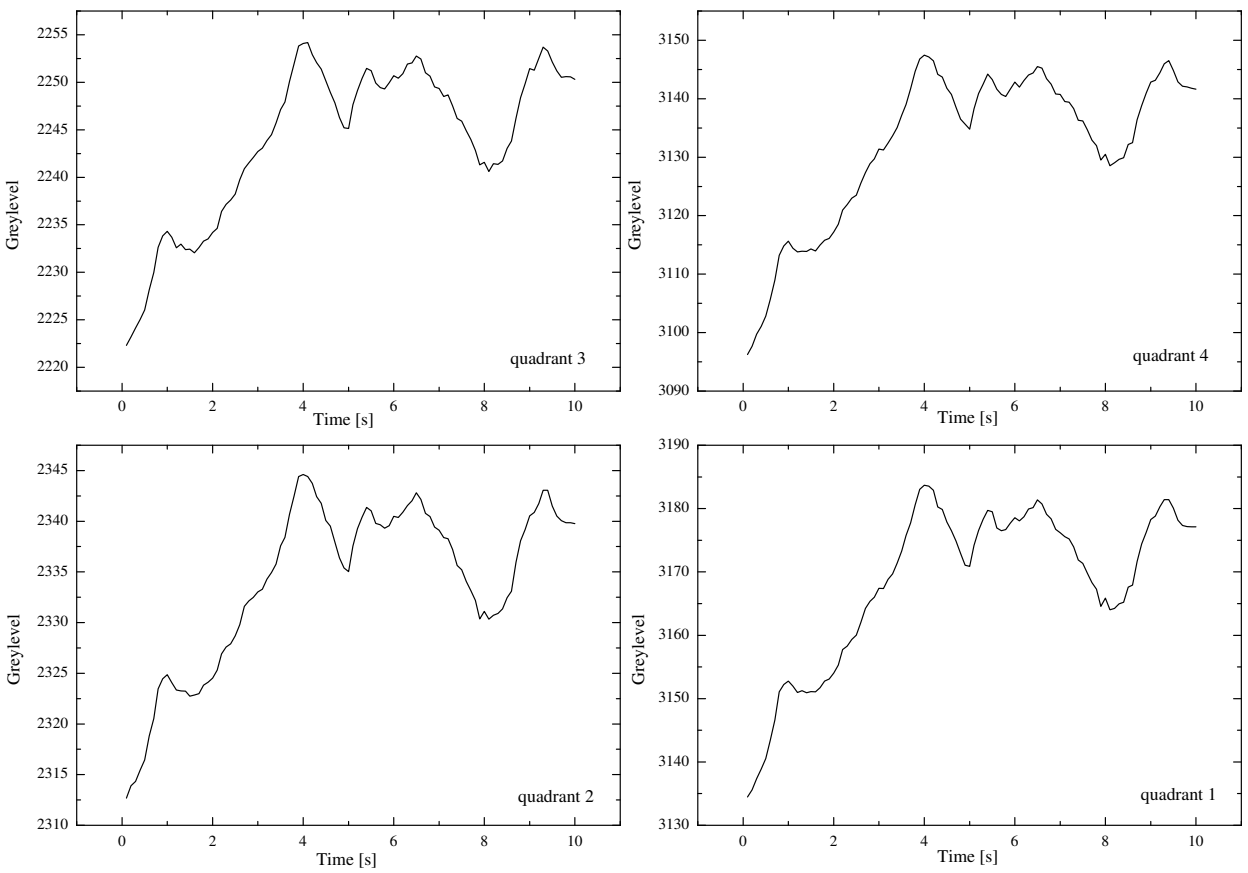
Figure 4.2: Comparison of intensity fluctuations in the four quadrants. The greylevel averaged over a quadrant is shown as a function of time, where one quadrant corresponds to an area of 27 cm² on the scintillator. The error due to counting statistics is below 1 greylevel.
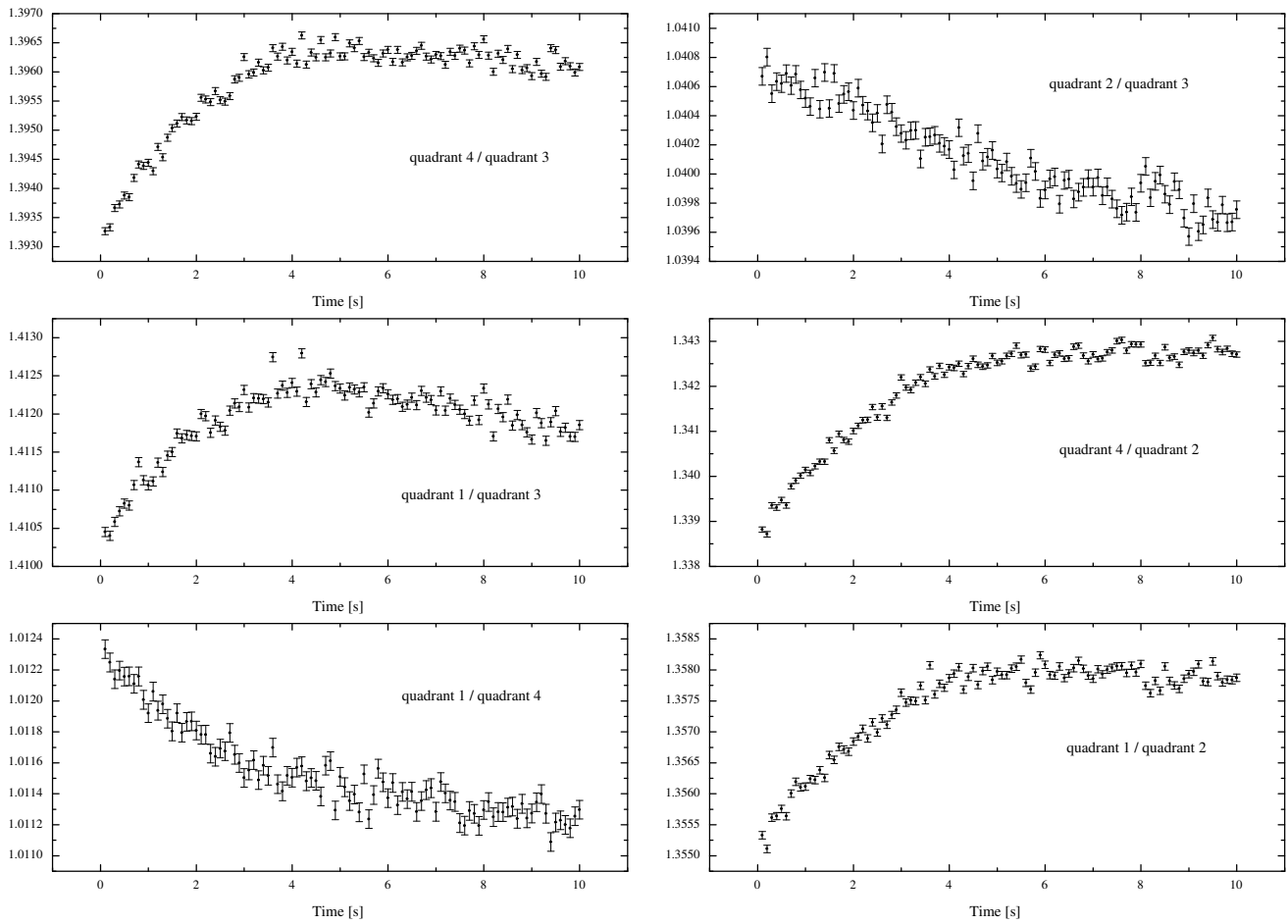
Figure 4.3: Quotients calculated from the measurements shown in Figure 4.2. The error bars represent statistical errors due to counting statistics. The intensity fluctuations differ on the 10^{-3} level between the four quadrants.

4.2 Statistical Errors

The principal source of statistical errors in our detector is the Poisson distribution of the number of neutrons coming from the reactor during the CCD's exposure time.

Other sources of statistical errors in the setup are photon noise behind the scintillator and readout noise of the CCD.

This section compares calculated and measured statistical variations and provides a method to calculate the error as a function of the greylevel in a radiographic image.

Our detector counts neutrons and neutron counting is governed by Poisson statistics. The variance σ^2 of the Poisson distribution equals its mean; the square root of the number of detected neutrons is therefore a good estimate of the statistical error of the measurement.

The raw data obtained from the camera are greylevel images. In our case, the greylevel of a pixel can be any integer number between 0 and 4095.

The greylevel G measured for a given pixel is related to the incoming flux I at the corresponding area of the scintillator by

$$G = I \; A \; t_e \; Q_{sc} \; N_\gamma \; Q_o \; L \; Q_{ccd} \; Q_{a/d}$$
(4.1)

with

I	incoming intensity
A	area seen by a pixel
t_e	exposure time
Q_{sc}	efficiency of scintillator, i.e. number of captured neutrons per incoming neutrons
N_γ	photons emitted per captured neutron
Q_o	reflectivity of mirrors
L	efficiency of optics
Q_{ccd}	quantum efficiency of CCD
$Q_{a/d}$	analog to digital ratio, i.e. inverse of the number of electrons that are necessary to increase the greylevel by one.

where

$$L = \frac{1}{[4F(1+m)]^2}$$
(4.2)

with the minification m and the lens's F-number F. The last equation is derived in Appendix A.

Typical values (cf. Section 3.1 and 3.2) are $I = (3.6 \pm 0.4) \times 10^9$ n cm^{-2} s^{-1} for the brightest spots of the open beam, $A = 3.6 \times 10^{-4}$ cm^2 for a distance of 1000 mm between camera and scintillator, $t_e = 35$ ms, $Q_{sc} = 0.3$, $N_\gamma = (0.7 \ldots 2) \times 10^5$ photons n^{-1} for a LiF-scintillator, $Q_o = 0.7$ for two Al-mirrors (estimated), $L = 1.1 \times 10^{-4}$ for $F = 1.2$ and $m = 19$, $Q_{ccd} = 0.4$ e$^-$ photon^{-1}, and $Q_{a/d} = 1/7.5e^- = 0.13$ greylevels per e$^-$ for the PCO Sensicam. The least accurate values are probably N_γ, as no data is available for precisely this scintillator, and Q_o which is only an estimate. The value of A will be further discussed below.

In order to measure the statistics of our detector we recorded 100 radiographies of the same object with a LiF scintillator (NE426) and all parameters as stated above. The object consisted of different absorbers that created areas with a varying attenuation of the beam. Some areas we left unshielded, so that we could measure the open beam. We took the images within 7 s, so the deterioration of the scintillator (cf. Section 4.1.1) was negligible. We had to correct for the systematic fluctuations of the flux (cf. Section 4.1.2). To do so, we multiplied each image by a factor, so that the average greylevel would be the same for all 100 images.

Now for each individual pixel we calculated its mean greylevel $\overline{G}$ and variance σ_G^2 over the 100 images. For a given pixel this is equivalent to making 100 independent measurements and then calculating the mean and the variance. This was done for 140000 pixels. For our measurement $\overline{G}$ ranged from about 60 to 3700 and σ_G^2 from 5 to 10000.

We will now discuss the relation of $\overline{G}$, σ_G^2, and the involved physical quantities.

First, let us consider only the brightest pixels with $\overline{G} > 3600$. These are about 1000 pixels. For these pixels $\overline{G} = 3612 \pm 14$. The distribution of the σ_G^2 for these pixels is shown in Figure 4.4. Fitting a Gaussian to the data yields $\sigma_G^2 = 670 \pm 100$. From this we can calculate the relative statistical error $r = \sqrt{\sigma_G^2} \, / \, \overline{G}$ to be[2]

$$r_{\text{measured}} = (7.2 \pm 0.5) \times 10^{-3}. \quad (4.3)$$

We consider the relative error rather than absolute errors because this makes a precise knowledge of most quantities in Equation 4.1 unnecessary. For example, a change in Q_o will equally influence σ_G and $\overline{G}$ and will therefore have no effect on the relative error r.
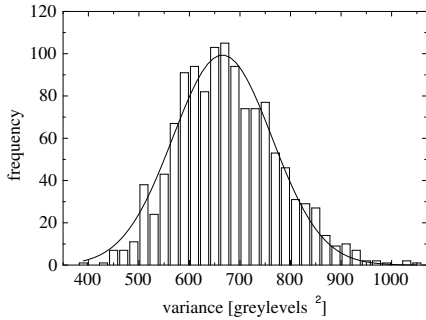

Figure 4.4: Frequency of variances for pixels with $\overline{G} > 3600$ with a Gaussian fit.

For the further discussion it is useful to write equation 4.1 as

---

[2]The error in σ_G^2 dominates the error of r. Gaussian error propagation yields

$$\Delta r_{\text{measured}} = \left| \frac{1}{2\sqrt{\sigma_G^2 \overline{G}}} \Delta \sigma_G^2 \right|.$$

$$G = \underbrace{I \ A \ t_e \ Q_{sc}}_{N_n} \ \underbrace{N_\gamma \ Q_o \ L \ Q_{ccd}}_{n_e} \ \ Q_{a/d}$$

$$(4.4)$$

with

N_n number of captured neutrons per pixel

n_e average number of electrons on CCD per captured neutron, i.e. average number of detected photons per captured neutron.

In this measurement we expect to capture on average $N_n = (1.4 \pm 0.2) \times 10^5$ neutrons per pixel in the brightest areas of the open beam (cf. Section 3.1). From counting statistics alone, one would expect a relative statistical error of[3]

$$r_{\text{n}} = \frac{1}{\sqrt{N_n}} = (8.5 \pm 0.6) \times 10^{-3}. \quad (4.5)$$

We will now consider additional error sources in the detection process.

Readout noise of the CCD is on the order of $\sigma_{\text{ro}} = 2$ greylevels, so the relative error is $r_{\text{ro}} = \sigma_{\text{ro}}/\overline{G} \approx 5 \times 10^{-4}$ and an order of magnitude lower than r_{n}.

The dark noise from the thermal creation of electron hole pairs in the CCD is another three orders of magnitude lower for such short exposure times.

On average, each captured neutron creates, through the intermediary photons from the scintillator, n_e electron hole pairs on the CCD. The process of counting neutrons by counting photons with electrons increases the relative error to

$$r_{\text{e}} = r_n \ \sqrt{1 + \frac{1}{n_e}} \qquad (4.6)$$

which is derived in Appendix A.

For n_e smaller than or about equal to one this can significantly deteriorate

---

[3]Here the error is given by

$$\Delta r_n = \left| \frac{1}{2} N_n^{-\frac{3}{2}} \ \Delta N_n \right|.$$

the relative error while for n_e much larger than one the error is mainly determined by r_n.

We can deduct $n_e = \overline{G}/(N_n\ Q_{a/d})$ from the measurement and get

$$n_e = 2.0 \pm 0.3. \qquad (4.7)$$

Plugging 4.7 into 4.6 yields the expected relative error. We find[4]

$$
\begin{aligned}
r_{\text{expected}} &= \frac{\sqrt{1 + \frac{1}{n_e}}}{\sqrt{N_n}} \\
&= (10.4 \pm 0.8) \times 10^{-3}.
\end{aligned}
\qquad (4.8)
$$

Note that this result depends only weakly on n_e and is almost fully determined by N_n.

Comparison of 4.3 with 4.8 shows a conflict between the measured and expected relative error. Surprisingly, we measure a lower relative error than we would expect.

The most likely explanation seems to be that effectively more neutrons contribute to the measurement than assumed in Equation 4.4. This way the relative error could be lowered. The beam intensity, exposure time, and efficiency of the scintillator are all well known. The area seen by a pixel was calculated geometrically by multiplying the on-chip pixel size ($9.9 \times 9.9\ \mu\text{m}^2$) with the square of the optical system's minification (19^2). Practically it is impossible to perfectly focus on the scintillator. Therefore, each pixel will gather some light from adjacent areas. Figure 4.5 illustrates how this effectively enlarges the area from which light falls on a pixel.

This consideration does not change the above estimation of n_e, as that is based on an average of many pixels. It does change the expected relative error

---

[4]The error is given by

$$\Delta r_{\text{expected}} = \left[\left(\frac{\Delta n_e}{2 r_e N n_e^2} \right)^2 + \left(\frac{r_e \Delta N}{2N} \right)^2 \right]^{1/2}$$

though. A pixel effectively sees a larger area. Hence, more neutrons contribute to the measurement and, according to 4.6, this reduces the relative error.

Assume an effective area of twice the geometric pixel area. Then the expected relative error of the above measurement is $r = 7 \times 10^{-3}$, in accordance with the experimentally observed relative error. Yet, the factor two is of course a pure guess.

So far, we considered only the brightest pixels because we know the beam intensity for them. Combining equations 4.5 and 4.3 will allow us to make predictions for the standard deviation σ_G of pixels depending on their greylevel G. It will also serve as a cross-check for the previous findings.

Very generally, we see from Equation 4.1 that G is proportional to some number N appearing in the detection process, be it neutrons, photons, or electrons.

$$G = \alpha N$$

The statistics are usually limited by the lowest number of information carriers in the process. We assume that N is that number. The standard deviation σ_G in repeated measurements of G will be proportional to the standard deviation σ_N in repeated measurements of N. The proportionality constant will be the same α as above.

$$\sigma_G = \alpha \sigma_N$$

Let $\overline{G}$ and $\overline{N}$ be the averages in a series of measurements. Assuming Poisson statistics for N yields

$$\left(\frac{\overline{G}}{\sigma_G} \right)^2 = \left(\frac{\overline{N}}{\sigma_N} \right)^2 = \overline{N}$$

and hence

$$\sigma_G^2 = \alpha\ \overline{G} \qquad (4.9)$$

so that a plot of the variance σ_G^2 as a function of $\overline{G}$ should show a linear function with slope α.

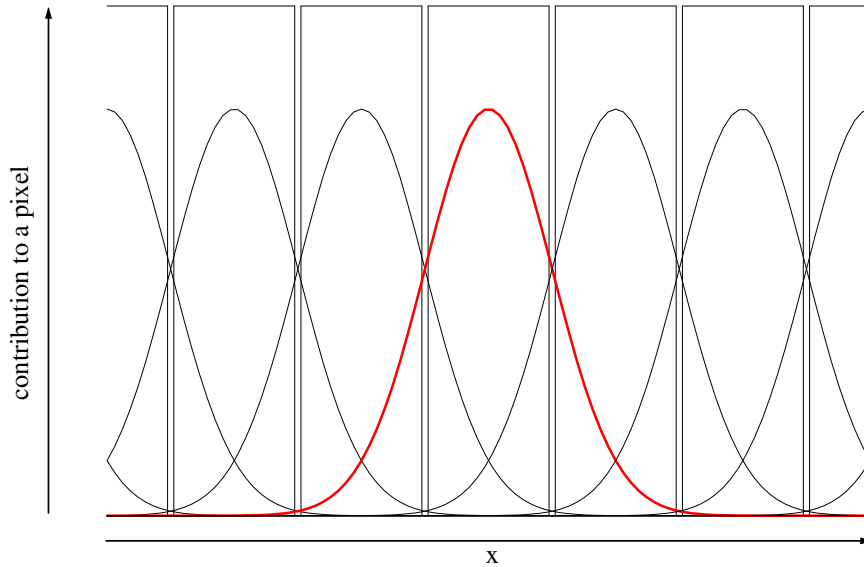Figure 4.6 shows such a plot for the measurement already discussed above.

Figure 4.5: This sketch schematically shows a line of pixels along the abscissa. On the ordinate is plotted how much the light coming from a certain spot contributes to each pixel. Instead of being perfectly separated (rectangular functions), pixels overlap and gather photons from adjacent areas (curved functions). This sketch is for illustrative purposes and the actual curves may look quite different.

Figure 4.7 shows the same data after binning it with respect to the mean greylevel.

First, we notice that indeed the variance shows a linear dependence on the greylevel. A linear fit yields $\alpha = 0.18$. Hence, with Equation 4.9 one would expect to find a variance of $\sigma_G^2 = 650$ for the brightest pixels with $\overline{G} = 3600$. This is in accordance with the measured values discussed above Equation 4.3. As those, it also conflicts with the expected values in Equation 4.8.

Second, the observed error of σ_G^2 is too large to be purely statistical. The reduced χ^2 for the fit in Figure 4.7 is 10^{-3}. A possible source of systematic errors in this measurement are non-uniformities of the scintillator. Two pixels may have the same average greylevel while at one of them the scintillator is good and there are few neutrons and at the other the scintillator is bad but there are many neutrons. Their fluctuations will then of course be different.

Third, this graph allows a prediction of errors from the greylevel of pixels. The slope α has to be determined for a given set of parameters, such as exposure time et cetera. In future measurements with the same parameters the error of a pixel with greylevel G can be estimated to be

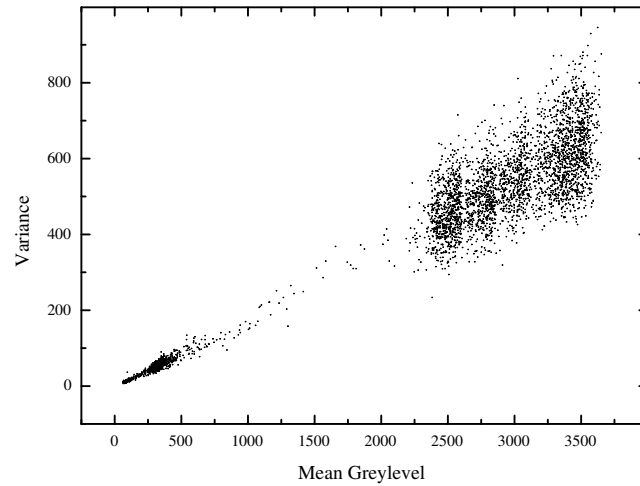$$\sigma_G = \sqrt{\alpha\, G}$$

as follows from Equation 4.9.

Figure 4.6: Scatter plot of the variance σ_G^2 as a function of the greylevel G. Each dot in the plot represents one pixel. The pixels cover a wide range of average greylevels because some parts of the scintillator were shielded by different absorbers. The density of dots varies because the shielded areas were not of the same size for all absorbers. For illustration purposes only about 4000 of the 140000 data points are shown.
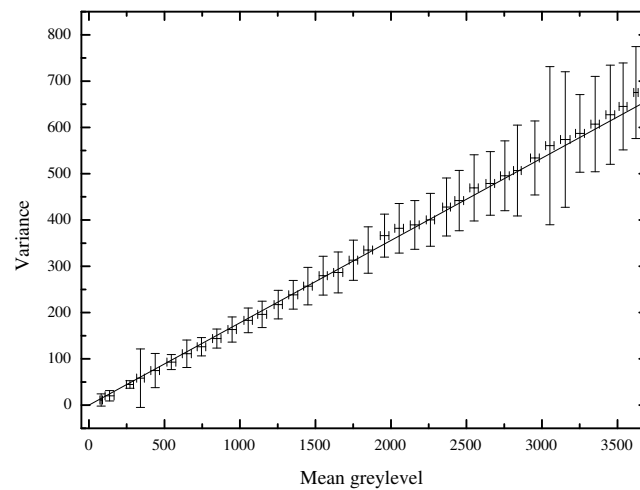

Figure 4.7: The data of Figure 4.6 after binning.

Limitations

Equation 4.6 might suggest that a patient experimenter only has to count neutrons long enough to reach any desired level of statistical error. Practically this is of course not true. If the CCD is exposed to long, it will produce overflow errors. Yet, one can often improve statistics by taking series of images and adding them up. If readout noise is negligible, this is equivalent to a longer exposure time.

If the desired time resolution forbids long exposure times but spatial resolution is of minor importance, binning pixels together is often a possibility to improve statistics.

The ability to correct systematic errors finally sets a natural limit on the attainable accuracy.

4.3   Contrast

The contrast of an image, that is, the possibility to distinguish small differences in the attenuation by the sample, is determined by how accurately the incoming and transmitted neutron intensity can be measured.

With a dimensionless attenuation coefficient, $M = \mu \Delta x$, Equation 2.1 becomes

$$I = I_0 \ e^{-M}.$$

If either μ or Δx are known, the other can be deduced from a measurement of M. This ultimately means measuring I_0 by counting N_0 neutrons and I by counting N neutrons.

Gaussian error propagation yields

$$(\Delta M)^2 = \left(\frac{\Delta N_0}{N_0}\right)^2 + \left(\frac{\Delta N}{N}\right)^2 \quad (4.10)$$

for the expected error of M. The relative errors of the measurements of N_0 and N are, if systematic errors are either negligible or can be corrected, given by Equation 4.6.

$$\frac{\Delta N}{N} = \frac{f_e}{\sqrt{N}} \quad\quad (4.11)$$

where $f_e = \sqrt{1 + 1/n_e} > 1$ is a constant of the detector (cf. Section 4.2). The same equation is valid for N_0. Plugging 4.11 into 4.10 gives

$$\Delta M = f_e \sqrt{\frac{1}{N_0} + \frac{1}{N}}.$$

Only attenuation differences larger than ΔM can be distinguished.

Note that N_0 and N may be very different. It is often possible to make very accurate measurements of the open beam and to make N_0 very large while experimental constraints, such as the intended time resolution, limit the accuracy of the transmission measurement and keep N small.

4.4   Spatial Resolution

For most samples the spatial resolution is limited by the beam divergence. Only for very flat samples that can be placed directly on the scintillator other factors start to play a role.

Let the sample be at a distance d from the scintillator. Due to the beam divergence Θ the position of some feature of the sample can only be determined within a precision of $\Theta \cdot d$, which is a good measure for the spatial resolution. For typical values of $d = 100$ mm and $\Theta = 6$ mrad, the spatial resolution is 600 μm.

Spatial resolution does get better as the sample is moved closer to the scintillator but is limited by the size of a pixel projected on the scintillator and the ability to focus on the scintillator. In our setup this sets a limit of about 200 μm.

4.5   Time Resolution

Technical constraints of the CCD camera and statistical considerations limit the time resolution.

After exposing the CCD it takes a certain time to read the information. Reading the entire chip of the PCO SensiCam

takes about 30 ms which limits the maximal frame rate, the frequency with which measurements can be repeated, to about 30 Hz. With typical exposure times of also about 30 ms, the frame rate is reduced to 15 Hz.

As the CCD is read line by line it is possible to increase the frame rate to about 150 Hz by limiting the region of interest, the part of the chip that is read, to a few lines. For long and thin samples with fast dynamics, such as liquids or gases in metal pipes, this is sometimes interesting. As the exposure time has to be very short to allow such fast repetitions, the result for the attenuation is very noisy.

Cyclic processes can be measured with very good time resolution and contrast if stroboscopic methods are employed. A trigger signal indicates each time that a certain moment of the process is reached. Electronics delay this signal by a time t_d which is initially set to zero. At each trigger signal the camera records an image. Increasing t_d allows to move forward in the process. This method also allows to record many images of the same moment in the process and add them up. This way statistics can be improved while keeping the individual exposure times short and time resolution high. The choice of steps for t_d and the exposure time determine the resolution of the process.

Practical considerations often limit the possible time resolution. Adding up very many images at many different times t_d may also take a lot of time. At some point the systematic errors due to scintillator degradation (cf. Section 4.1.1) prohibit further improvements.

Ultimately the scintillator afterglow time, typically about 100 μs for a LiF scintillator, sets a limit on time resolution.

4.6 Image Intensifiers

Using image intensifiers for neutron radiography is often discussed and some groups indeed opted for image intensifiers in their detectors. In Section 4.2 we come to the conclusion that neutron statistics determine the statistics of the measurement. As an amplifier cannot by itself increase the signal-to-noise ratio, it would not improve our setup. We have compared the statistical fluctuations of measurements with and without an intensifier. Figure 4.8 shows that a setup with an intensifier at high gain has the same statistics as a setup without intensifier. At a low gain the intensifier adds noise. Image intensifiers may improve the signal if they allow to use scintillators with much higher efficiency, shift the photon wavelength to a region where the CCD is more efficient, or if their geometry allows to collect more photons than a regular objective. As Equation 4.6 shows, the latter is only interesting if the number of photons detected per absorbed neutron is about one or lower.

4.7 Data Treatment

This section provides a summary of the typical steps in the data evaluation of a dynamic radiography. Special circumstances may often make it necessary to adjust the procedure.

Image Acquisition
Three types of images have to be recorded. Images of the sample, images of the open beam, and dark images without neutrons. Recording many images usually improves statistics.

Summing
If many images were recorded, the first step is to sum them up in one image.

Dark Image Substraction
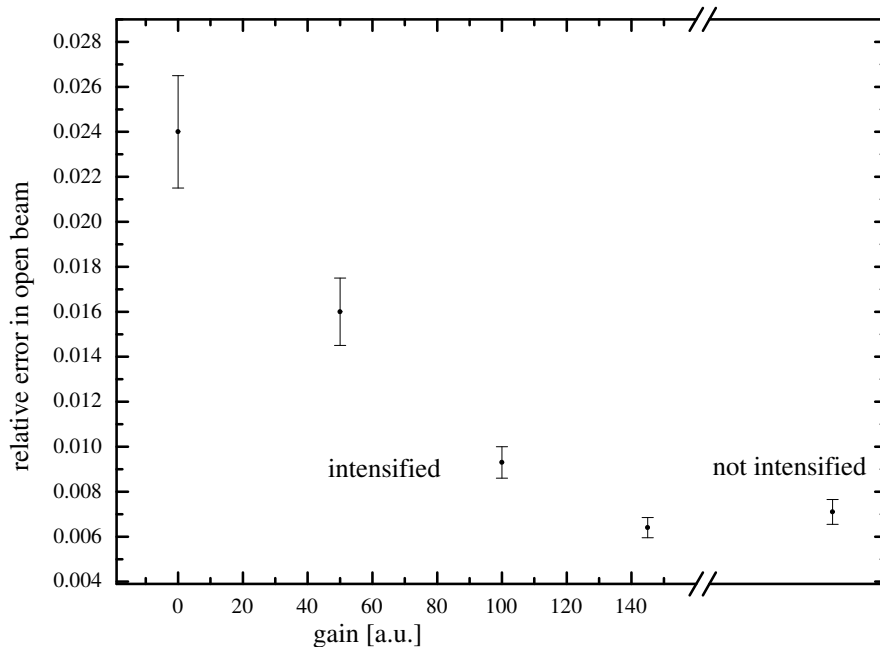CCDs have a positive offset greylevel

Figure 4.8: Comparison between detectors with and without image intensifier. On the left side are plotted the statistical fluctuations observed in a measurement of the open beam with the Pi-Max:1300-E intensified camera from Roper Scientific [Rop] and on the right side is plotted the result for the PCO SensiCam without intensifier [PCO]. Both measurements were performed with the same NE426 scintillator and equivalent exposure times.

that will be returned even when no photons were detected. This avoids the occurrence of negative greylevels. The dark images measure this offset and need to be subtracted from all images of the open beam and the sample. Care has to be taken if in the previous step different numbers of images were summed.

Intensity Fluctuation Correction

The fluctuations of the beam intensity are corrected by multiplying images globally with constant factors chosen according to section 4.1.2.

Scintillator Decay Correction

If the measurement took so long that the scintillator deteriorated during the measurement, the methods described in 4.1 need to be applied. If possible, this should be avoided.

Open Beam Division

According to Equation 2.1 the beam attenuation is given by the natural logarithm of the image of the sample divided by the image of the open beam.

Chapter 5

Measurements

We report here mainly the results from measurements concerning the visualization of gasoline inside combustion engines. The second section presents results from measurements in three other areas: two-phase flow in a small steel pipe, water transport in building materials, and water transport in a biochemical sample.

Please find attached to this paper a CD with movies of dynamic radiographies.

5.1 Combustion Engines

Hydrogen's large scattering cross section gave rise to the idea of visualizing the gasoline distribution inside combustion engines with neutron radiography. We present three dynamic radiographies: of a stand-alone standard diesel injection nozzle, of a small running gasoline engine, and of an externally driven car engine. Experiments with the injection nozzle showed the feasibility of the project. The experiments with the running engine still have too large systematic errors. The car engine showed that the step from model engines to engines of industrial interest will probably be small.

Results from other measurements in this field can be found in e.g. [Bru01], [Fer02], and [Bru02].

5.1.1 Introduction

Cars and trucks consume vast amounts of fuel with all the environmental, economic, and political implications. Neutron radiography could possibly contribute to research efforts to reduce fuel consumption.

The distribution of gasoline in the cylinder is a major factor for the engine's efficiency (see e.g. [Zha99], [SFB01]). Various measurement methods, most based on light, have been conceived to measure this distribution [SFB01]. Significant changes to the engine, such as replacing metal parts with glass, are often necessary and limit the interpretation of results. Neutron radiography could supplement these methods by measuring the gasoline distribution inside running engines without changes.

Modern engines are typically made of aluminum alloys. They have relatively small attenuation coefficients and are transparent in neutron radiographies. Steel is less transparent and requires longer exposure times. Gasoline and diesel consist mostly of hydrogen. Hydrogen has a large scattering cross section for neutrons and is therefore opaque in radiographies.

We estimate the beam attenuation due to the fuel. Let C be the engine's consumption per unit time and cylinder and let f be the engine's speed in revolutions per unit time. Then in each cycle

31

of the four-stroke process the volume

$$v = \frac{C}{f/2}$$

of fuel enters the cylinder. We assume the fuel to be evenly distributed over the volume V/K, where V is the cylinder's volume and K is a compression factor given by the position of the piston. Let n be the number density of hydrogen atoms in the fuel and σ the total cross section of hydrogen. The attenuation coefficient is then given by

$$\mu = \frac{Kvn\sigma}{V}.$$

Let d be the cylinder's diameter. At the middle of the cylinder the fuel attenuates the beam by a factor

$$A = 1 - \exp(-\mu d) \approx \frac{2CKn\sigma d}{fV}. \quad (5.1)$$

To estimate n we assume the gasoline to consist of octane, which contains $N_H = 18$ hydrogen atoms and has a molar mass of $M \approx 114$ amu mol^{-1}. With Avogadro's number N_A and the density of gasoline $\rho = 0.8$ g cm^{-3} we get $n = N_A\, \rho\, N_H/M \approx 8 \times 10^{22}$ cm^{-3}.

Assume an average car going 100 km/h. The 4-cylinder 1.5 l engine runs at about 2500 rpm and uses 8 l/h. The injection volume $v \approx 30$ mm^3 and the piston diameter $d \approx 8$ cm. For a typical compression of $K = 1\ldots10$ we get an attenuation of $A = 0.5\ldots5\%$. Depending on the required spatial resolution it is possible to measure the attenuation with a relative error of 0.1% within some seconds to minutes exposure time.

5.1.2   Injection Nozzle

We made dynamic radiographies of the spray from a standard diesel injection nozzle[1].

The nozzle sprayed some milliliters of probe oil with high pressure perpendicular to the beam. This was repeated with a frequency of 2 Hz. Because of the explosion hazard we used nonflammable probe oil that is otherwise very similar to diesel or gasoline.

We applied the stroboscopic method described in Section 4.5. At 6 time steps, 100 μs apart, we recorded 5000 images with an exposure time of 100 μs. Open beam images were recorded with the same total exposure time. Binning was two by two pixels. The accuracy of the measured attenuation is about 0.2% (cf. Section 4.3).

We treated the data according to Section 4.7 and corrected against beam intensity fluctuations. Scintillator degradation was very homogeneous and could be corrected with the help of repeated open beam measurements.

Figure 5.1 shows the oil spray expanding from the nozzle. Attenuation by the oil is $(4\pm2)\times10^{-3}$, corresponding to the gasoline in a car engine prior to compression.

5.1.3   Running Engine

We made dynamic radiographies of an of-the-shelf 2 kW, 156 cm^3, one-cylinder four-stroke gasoline engine. An electricity generator served as an exhaust break. The engine was made of aluminum and worked with a carburetor. Minor changes made the cylinder more accessible. Figures 5.2 and 5.3 show photographes of the engine.

The exhaust gases were cooled in 5 m long tombac tubes before entering the reactor's system of radioactive waste gases. Rubber pads damped the engine's vibrations.

The gasoline consumption was 0.8 l/h when idling and 1.1 l/h under full load.

---

[1]These experiments were carried out together with Johannes Brunner from the Technical University of Munich. We thank the Robert Bosch GmbH for supplying the injection nozzle and accessories.
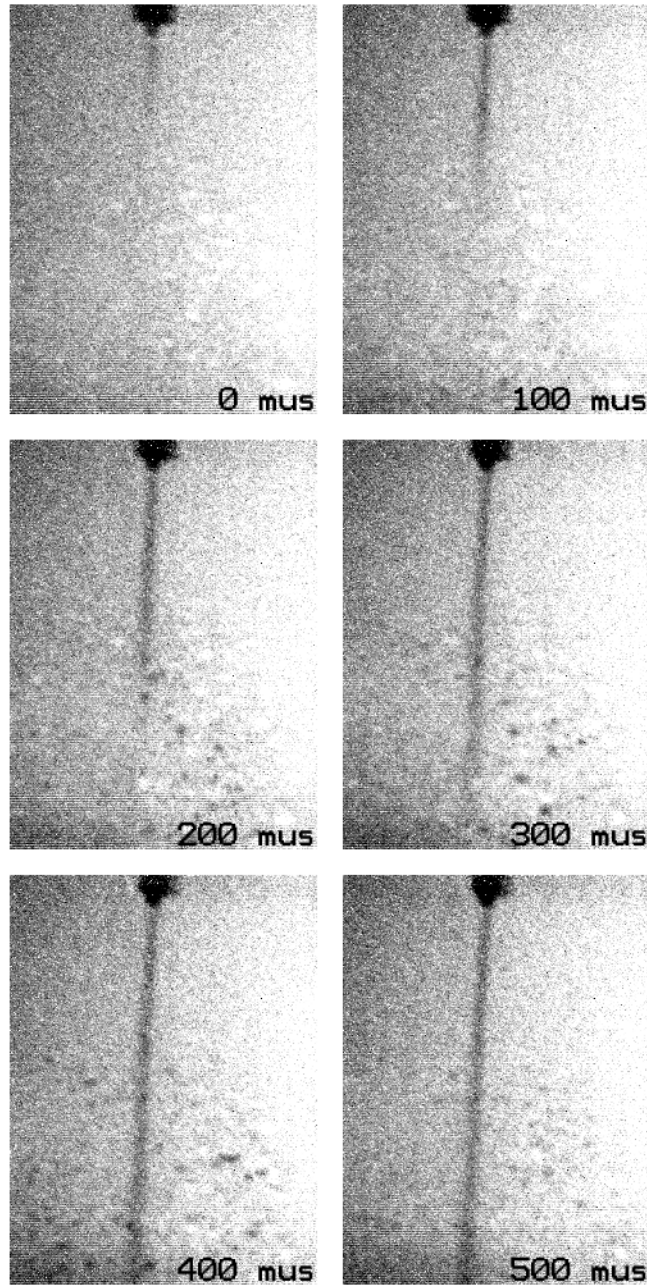
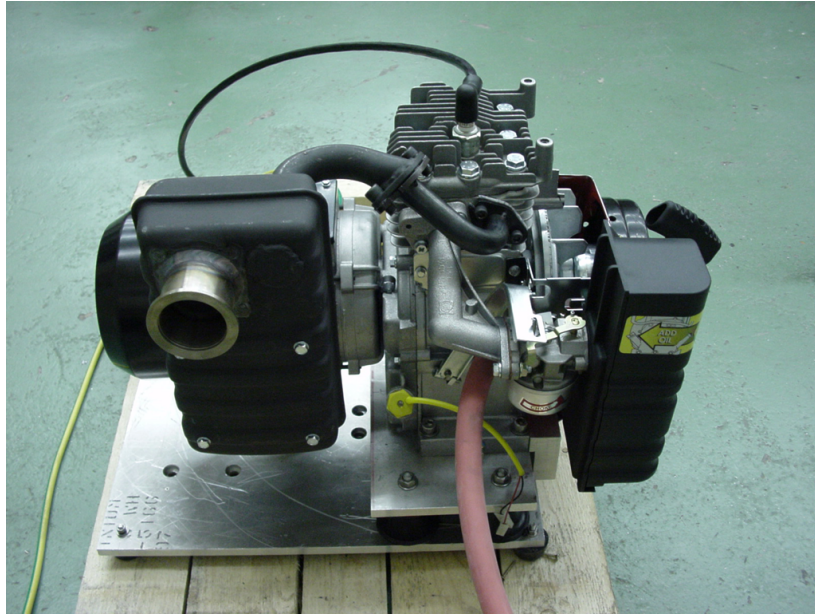Figure 5.1: Oil spray from an injection nozzle. The field of view is 62 mm wide and 82 mm tall.

Figure 5.2: Side view of the engine with the cylinder on the right and the electricity generator on its left. The entire setup is about 50 cm wide.
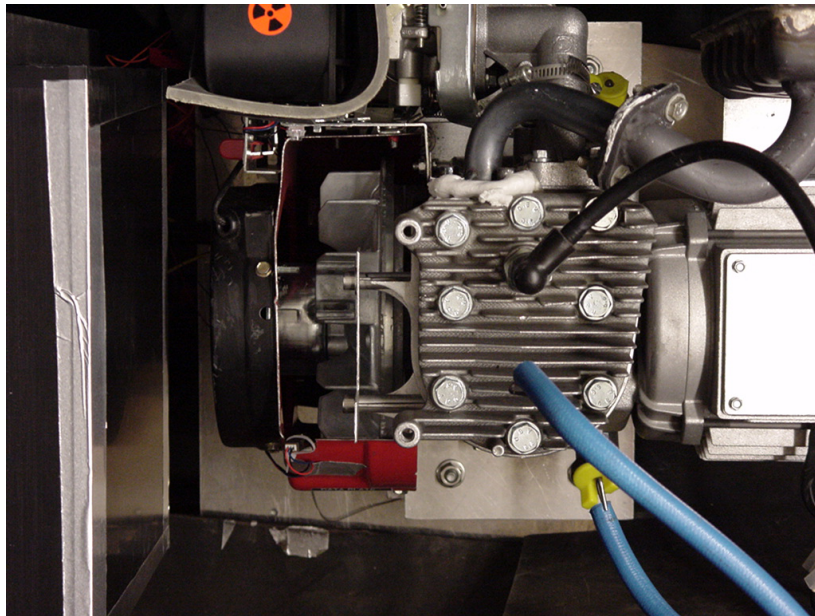

Figure 5.3: Top view of the engine. The beam comes from the right and the detector can be seen on the left.

The engine ran at 3000 rpm; a full four-stroke cycle took 40 ms. The maximum compression rate could be estimated to about 10. Equation 5.1 predicts, depending on the compression, a beam attenuation of 2×10^{-3} to 2×10^{-2} due to the gasoline.

Again we applied the stroboscopic method. We synchronized engine and detector with a trigger signal from a light barrier on the shaft. We measured the 40 ms cycle in 40 steps of 1 ms and for each step we recorded 30 images with 1 ms exposure time. A programmable gate generator allowed to complete the measurement within about 80 s.

We treated the data according to Section 4.7 to correct against beam intensity fluctuations, while the short measurement time made corrections against scintillator degradation unnecessary.

Figure 5.4 shows eight of the images. The attached CD contains the entire series as a movie.

The relative error on the beam attenuation is between 1% and 2% for individual pixels in the regions of interest. It is too large to observe an effect due to the gasoline. Binning 100 pixels reduces the relative error by a factor 10.

Figure 5.5 shows the average transmission as a function of time in two regions of 100 pixels. In one region, between cylinder and valve, one would expect to see an effect from the gasoline. In the other region, above the cylinder, there is no gasoline. Both regions show similar fluctuations. We assume that these fluctuations are due to the engine's vibrations with about 1 mm amplitude. So far, these vibrations prevented conclusive measurements of the attenuation due to gasoline. Software routines that correct the vibrations still produce too much noise.

Because of gadolinium's large cross section we considered Gd 2-ethylhexanoate (25% in toluene), which is commercially available and soluble in gasoline, as a contrast agent. Un-fortunately the high molecular mass of $M \approx 650$ means a number density of only about 10^{21} cm^{-3} and each molecule contains only one Gd atom. A 1%-solution in gasoline would have a Gd density of 10^{19} cm^{-3}, which is about four orders of magnitude lower than the H density. As the cross section of gadolinium is only about 500 times larger than that of hydrogen, this would not significantly increase the attenuation.
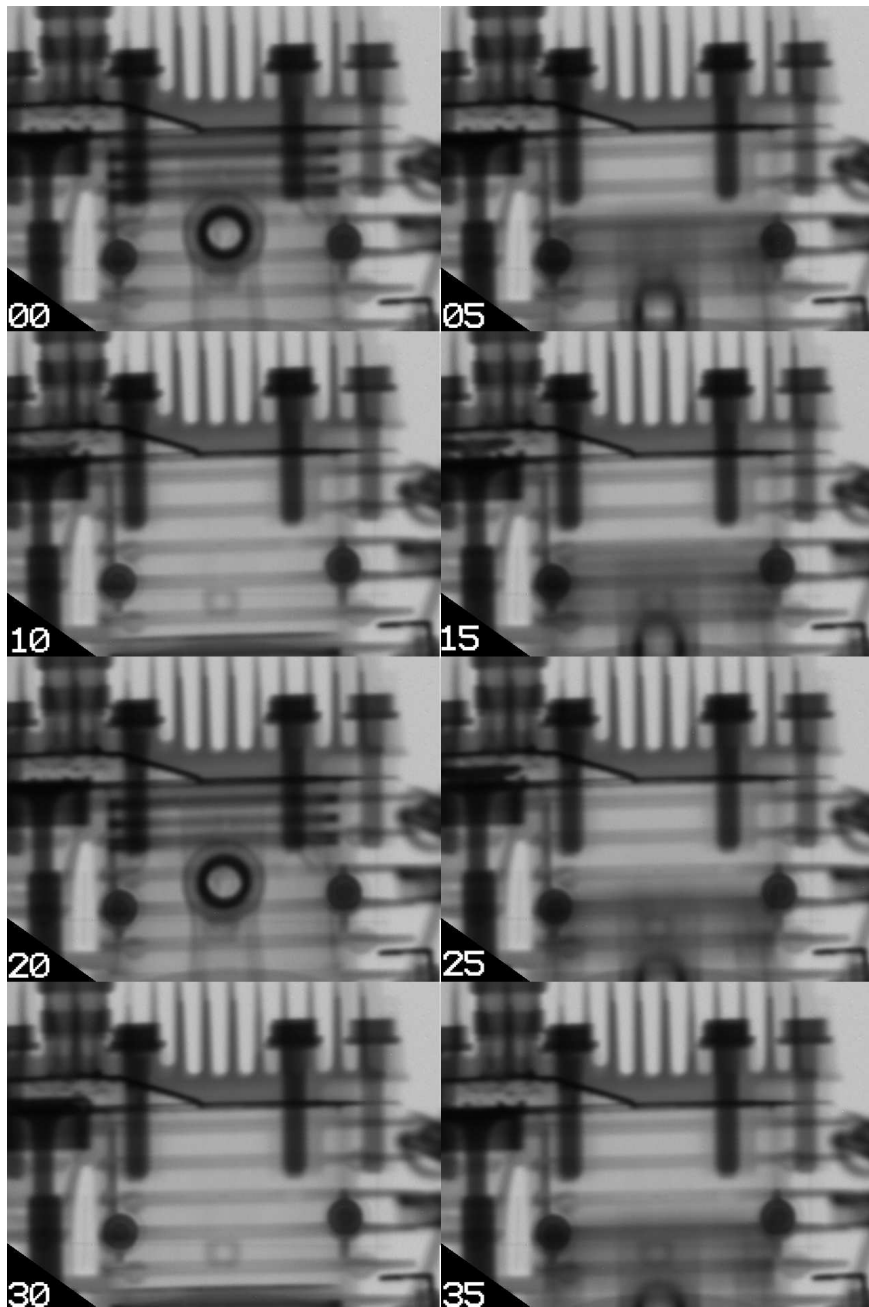
Figure 5.4: Dynamic radiography of a running combustion engine. Each image shows the time t in milliseconds. In the center of the images one can see the piston moving up and down. On its left are two valves, one behind the other. Note that the inlet valve is somewhat larger than the outlet valve. The compressed fuel-air mixture ignites at $t = 0$ ms and expands until $t = 10$ ms. Then the exhaust gases are ejected and fuel enters the cylinder again. At $t = 35$ ms the mixture is compressed before the process repeats. The piston's diameter is about 6.5 cm.
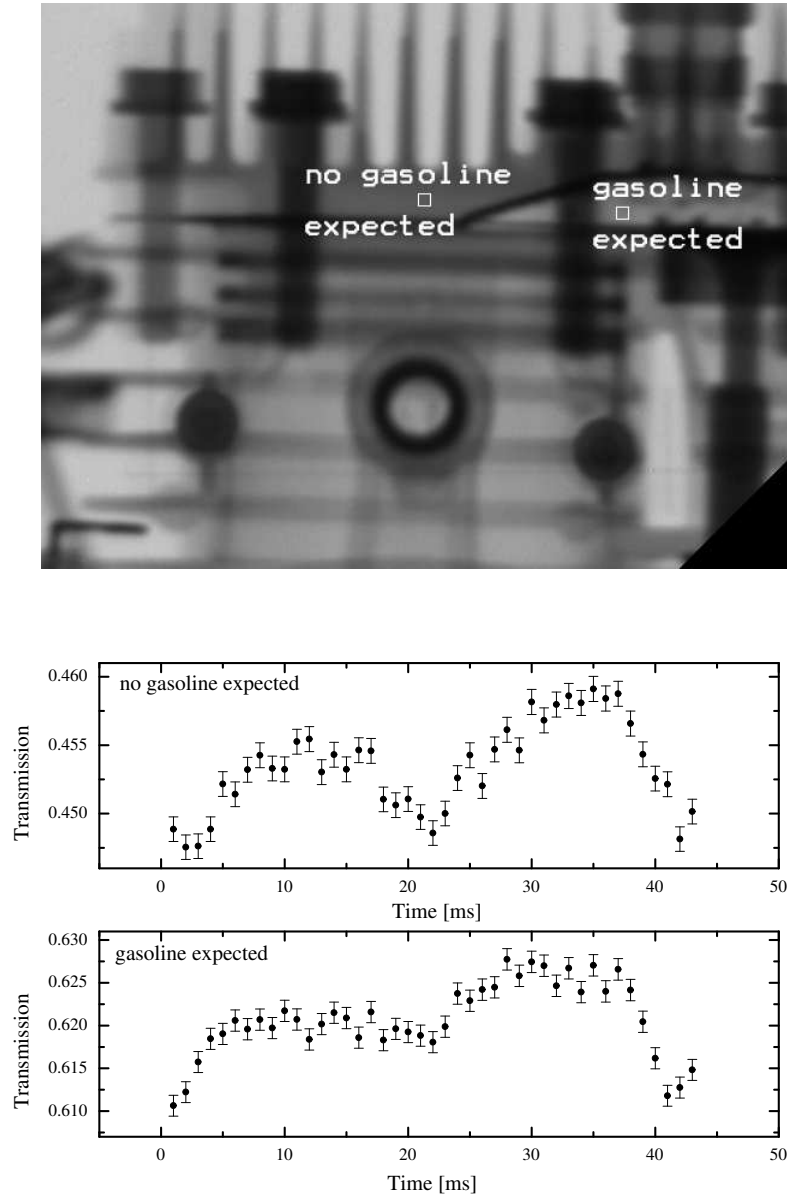
Figure 5.5: Transmission as a function of time during one engine cycle. Transmission is shown for one region where gasoline is present and one region without gasoline. The areas are 100 pixels, i.e. 3.5 mm^2 large. We attribute the visible fluctuations to the engine's vibrations. These have so far prevented the visualization of the gasoline.

5.1.4   Car Engine

From the standpoint of neutron radiography the differences between the small engine of the last section and a car engine are small. All considerations about beam attenuation and time-scales remain the same. Technically a car engine is more demanding with regard to the exhaust gases and the exhaust break for example. To gain first experiences we made a dynamic radiography of a car engine that was driven by an electrical motor and not running by itself.[2]

We used a four-cylinder, 2 l engine from the BMW 3 series. Apart from linking it to an electrical motor, the engine was not changed.

It ran at 1000 rpm and images were recorded every millisecond. Every time 150 images of 0.2 ms exposure time were added on-chip before reading the CCD. For these measurements we used the intensified camera Pi-Max:1300-E from Roper Scientific [Rop].

Figure 5.6 shows six images. The whole series can be found on the attached CD. The results are similar to those for the small running engine. Moving parts in the car engine are sharper because of the shorter individual exposure times and the three times lower speed of the engine.

---

[2]These experiments were carried out in close cooperation with Eberhard Lehmann and Gabriel Frei from the Paul Scherrer Institute and Burkhard Schillinger from the Technical University Munich. We thank the BMW AG for supplying the engine.
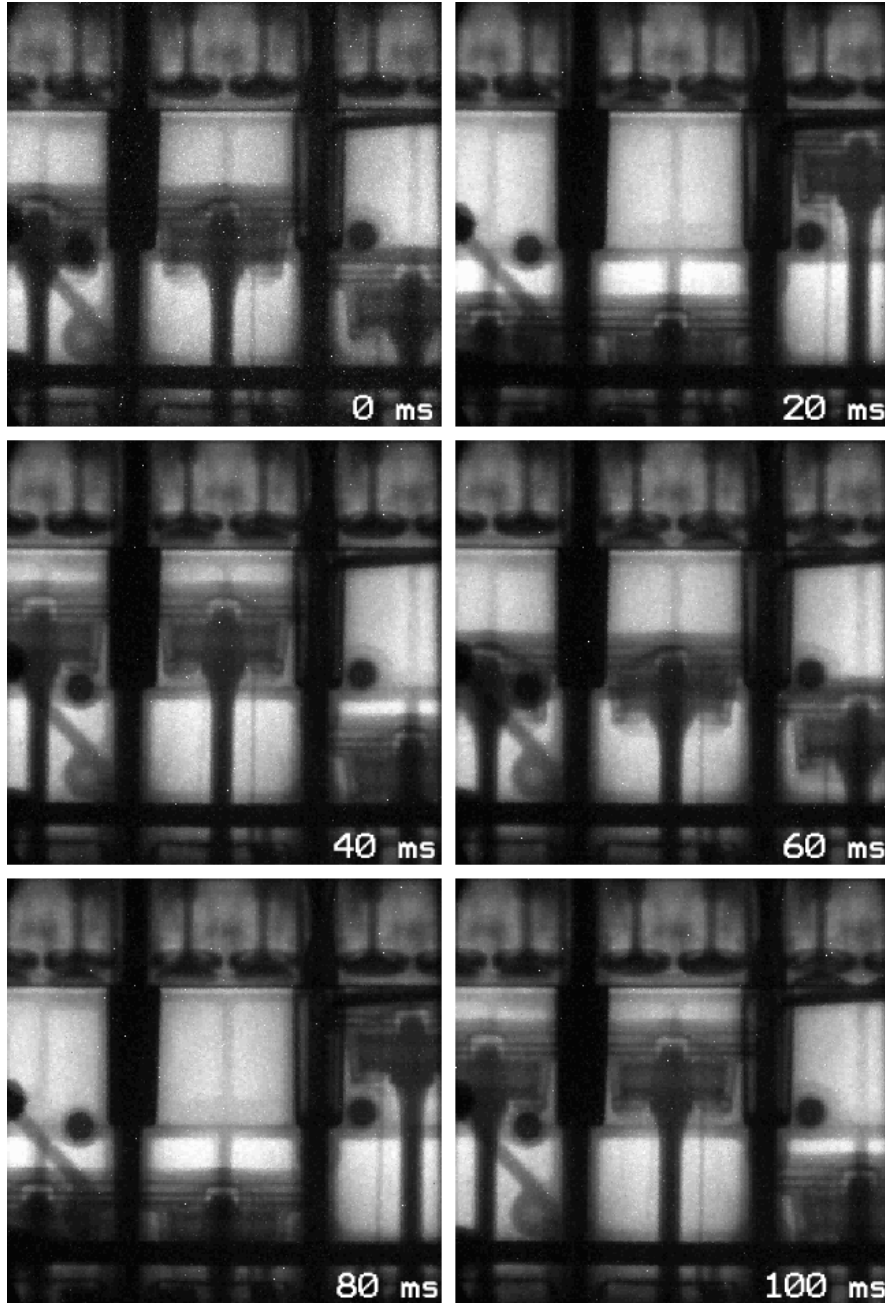
Figure 5.6: Car engine driven by an electrical motor. Note the oil beam below the center and right piston. It serves to cool the pistons.

5.2   Further Measurements

During the three reactor cycles of 2003 we did measurements with a growing number of external users. To show the wide range of applications of neutron radiography, three examples are discussed below.

5.2.1   Two-Phase Flow

The visualization of two-phase flow with neutron radiography is an active field of research [Tak99] [Asa03]. It exploits the higher attenuation in the liquid than in the gaseous phase.

Among the applications are miniature heat exchangers and fuel cells. For the former a more detailed understanding of boiling heat transfer is necessary [Mar97]. The latter require insight into flow characteristics and bubble formation [Bew03] as well as flooding and membrane drying [Cos01].

We have recently made dynamic radiographies of pentane boiling in a small steel tube as it is used for heat exchangers.[3] Pentane flowed constantly into a steel tube with an inner diameter of 1 mm and an outer diameter of 2 mm. The tube could be heated with an electrical current. A thermocouple allowed to measure the temperature. Images of 10 ms exposure time were taken at a rate of 64 Hz.

Figure 5.7 shows first results. First the tube is filled entirely with liquid pentane. Then it is heated to above 70°C, far beyond pentane's boiling point of 36.1°C. The superheated liquid evaporates very rapidly and the temperature drops.

The data have not yet been analyzed in detail but it is already clear that gas and liquid flow is a fruitful field of application for dynamic neutron radiography.

5.2.2   Building Materials

Water is opaque in neutron radiographs because of hydrogen's large scattering cross section. Therefore, neutron radiography allows to visualize water transport particularly well.

We present here first results from experiments on the water penetration in building materials.[4] A detailed analysis of the results lies beyond the scope of this paper but the experiments are exemplary of the possibilities of neutron radiography. More detailed preliminary results can be found in [Mas03].

Water penetration is one if not the major factor in the destruction of building materials [Lat62], making the process a continuous topic of research. Neutron radiography can contribute to this with time-resolved measurements and three-dimensional computer-tomography.

We investigated porous natural building stones from Belgium, like sandstone and limestone, as well as YTONG, a porous concrete [YTO]. Water penetration was measured as a function of time for different porosities and some water repellents were tested.

Figures 5.8 and 5.9 show two examples. The attached CD contains them as movies.

We placed the YTONG sample in a petri dish that was filled with water at time zero. Then we recorded a tomography every few minutes and reconstructed the attenuation in three dimensions. The images show how the water (dark) slowly rises in the initially dry sample through capillarity.

In Figure 5.9 one can see a RILEM tube attached to the sandstone sample [RIL]. This is a standardized device to measure the water penetration in masonry. In the first image both sample and

---

[3]These experiments were done together with Fredrik Lundell and Kathryn Oseensenda from the Commissariat à l'Énergie Atomique in Grenoble.

[4]These experiments were done together with B. Masschaele, M. Dierick, and S. Delputte from the Department of Subatomic and Radiation Physics at the Ghent University and V. Knudde from the Department for Geology and Soil Science at the Ghent University.
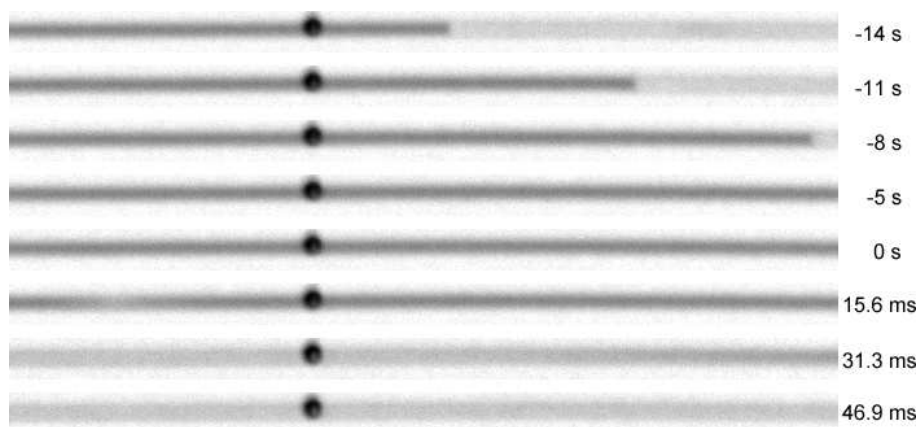
Figure 5.7: Pentane flowing from left to right in a small steel tube. After filling the tube the liquid is superheated and then evaporates rapidly. The length of the pipe is about 5 cm. The dark dot is a thermocouple.
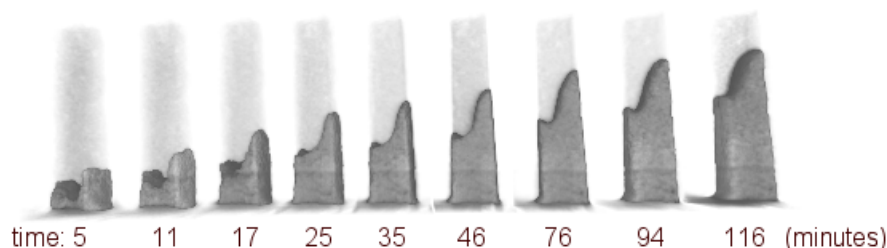

Figure 5.8: Tomographies of water (dark) rising in YTONG by capillarity. The sample is about 5 cm tall. The asymmetry of the water front is probably due to the experimental setup and not due to an asymmetry of the sample.

tube are dry. Then water is filled into the tube and enters the stone.

5.2.3 Myelin

We have made dynamic radiographies of the water transport into a sample of egg yolk lecithin, a molecule consisting of a hydrophilic headgroup and a hydrophobic part.[5] Similar molecules are well-known from cell membranes, where they form a bilayer. They play a role both in nature and in industrial applications, such as detergency. In our case they form a lamellar phase which shows swelling when brought in contact with water [Buc99].

Figure 5.10 shows a micrograph of "myelins". These are multi-bilayer tubules, typically about 10 μm in width, that grow out of the initial lamellar phase as it swells. One part of the research in this field aims at understanding the kinetics of the dissolution process. Neutron radiography can contribute to this research with its ability to distinguish hydrogen and deuterium.

Figure 5.11 shows a neutron radiog-

---

[5]These experiments were done together with Eva Herzig and Stefan Egelhaaf from the University of Edinburgh.

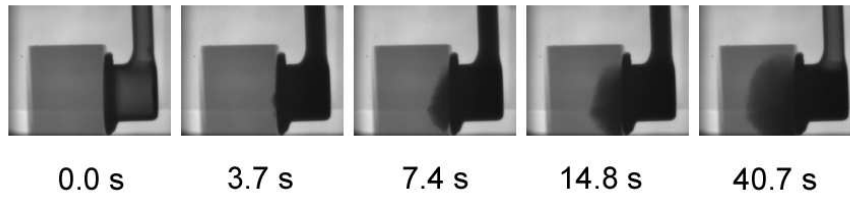| 0.0 s | 3.7 s | 7.4 s | 14.8 s | 40.7 s |

Figure 5.9: Water penetration in sandstone. The sample is about 4.5 cm tall. Water enters through the RILEM tube attached on the right side.

raphy of a sample of egg yolk lecithin containing 15% water. Two 1 mm thick boron-free glass plates held the 0.5 mm thick sample. The glass was held by plexiglass that also sealed the sample cell. Liquids could be injected from the top of the cell. We added heavy water (D_2O) to the lecithin sample. D_2O is, contrary to light water and the lecithin, relatively transparent for neutrons.

Figure 5.12 shows preliminary results on the neutron transmission along the black line in Figure 5.11. Transmission is shown for different times after the injection of D_2O. The estimated errors stem from the scintillator degradation and can probably be reduced significantly in a more detailed data evaluation. One can see how the initially sharp sample border is softened. Supposedly, myelins grow out and D_2O enters the sample.

The good visibility of water in neutron radiographies has many more potential applications. For example, we also studied water transport in samples of sand and soil. An advantage of neutron radiography over the more common X-ray radiography in this field [Wil02] is the high contrast even in our samples of up to 150 mm thickness.
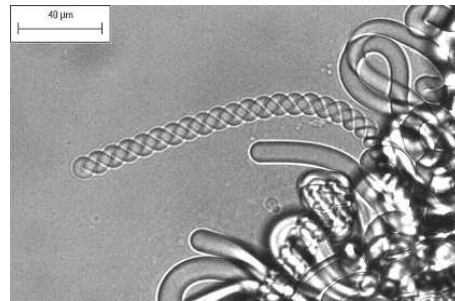

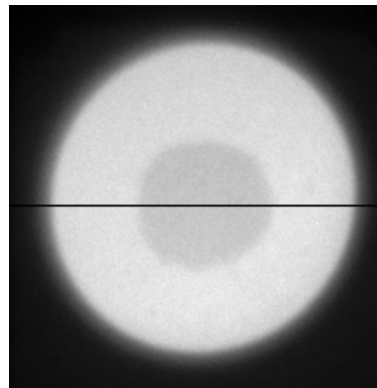Figure 5.10:   Micrograph of myelins. Source: [Buc99]

Figure 5.11: Neutron radiography of egg yolk lecithin containing 15% H_2O (center) surrounded by D_2O. The sample is about 12 mm wide.
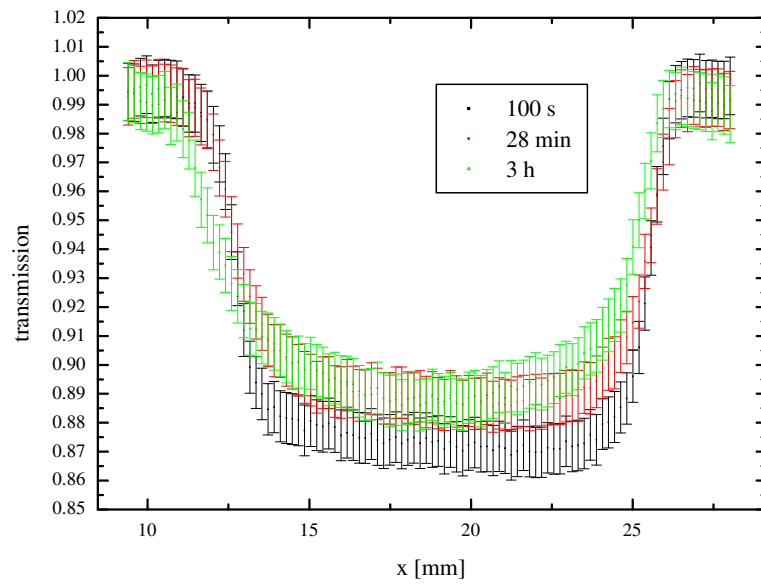
Figure 5.12: Neutron transmission of a sample of egg yolk lecithin (center, low transmission) dissolving in D_2O (borders, high transmission). The curves represent different times after D_2O was injected into the sample cell.

Chapter 6

Outlook

The properties of the new neutron radiography and tomography facility *Neutrograph* have been discussed. The high flux of 2.9×10^9 n cm^{-2} s^{-1} and the moderate divergence of 6 mrad allow dynamic radiographies of processes in the millisecond range with a spatial resolution of about 0.5 mm.

We found scintillator degradation and systematic intensity fluctuations to be the largest sources of systematic errors. Counting statistics determine the statistical errors.

The spray from an injection nozzle could be visualized and dynamic radiographies of a running model-sized combustion engine, as well as an externally driven car engine, were recorded. Other measurements included two-phase flow in a small steel tube, water penetration in building materials, and water transport into a biochemical sample.

Throughout 2003 *Neutrograph* has developed away from a pure test experiment towards a user instrument. While for the first reactor cycle only two users requested beam time, there were six requests for the last reactor cycle of 2003.

Further developments are necessary to make *Neutrograph* a user-friendly tool. Sample and detector positioning could be automatized. Enlarging the casemate would allow to investigate large samples like car engines more easily. Prolonging the casemate towards the reactor wall would also allow the installation of a second sample position with better divergence. The development of software that integrates camera and step motor control for tomographies etc. has started. It could be combined with software for online tomographic reconstruction. Furthermore, the data treatment routines could be integrated into a single program.

Scintillator degradation is an unsolved problem. If stable scintillators cannot be found, a correction mechanism is needed.

The ambitious project of fuel visualization in combustion engines will be pursued further. Fuel cells and material science are other fields of high potential.

Neutron radiographers and engineers could mutually profit from a closer cooperation. Neutron radiography, still being a relatively young and widely unknown method, needs to become known to a larger group of applied scientists. In turn, it offers an excellent tool for destruction-free testing. Therefore experiments are planned together with FaME38, the joint facility for materials engineering of the Institut Laue-Langevin and the European Synchrotron Radiation Facility.

In the long term the beam position might be used for extra-corporal boron neutron capture therapy in parallel. This novel technique employs neutrons to destroy cancer cells that were previously marked with boron.

Appendix A

Derivations

Solid Angle

We derive Equation 4.2,

$$L = \frac{1}{[4F(1+m)]^2}$$

which relates the fraction L of the photons arriving on the CCD with the lens's F-number F and the optical system's minification m.

Assume that the scintillator emits photons isotropically into the full solid angle of 4π. Let d be the diameter of the lens and d_o the object distance, i.e. the distance between scintillator and lens. The fraction of photons arriving at the lens is

$$L = \frac{\pi(d/2)^2}{4\pi d_0^2}. \qquad \text{(A.1)}$$

Let f be the focal length of the lens and d_i the image distance. The thin lens equation,

$$\frac{1}{f} = \frac{1}{d_o} + \frac{1}{d_i}$$

yields

$$m = \frac{d_o}{d_i} = \frac{d_o}{f} - 1.$$

Together with the F-number's definition

$$F = \frac{f}{d}$$

and A.1 we get Equation 4.2.

Relative Error

Here we derive Equation 4.6,

$$r_e = r_n \sqrt{1 + \frac{1}{n_e}}$$

which relates the expected relative error r_e of a measurement with the error r_n due to neutron statistics and the average number of electrons collected on the CCD per absorbed neutron n_e. The argument is basic but many textbooks skip it as in most experiments either the number of initial particles or the number of electrons in the detector dominates the statistics. In our experiment these numbers are of the same order of magnitude, so neither can be neglected.

Imagine a series of n measurements, where in the ith measurement N_i neutrons are absorbed in the scintillator. Let $P(E_i|N_i, n_e)$ be the probability to collect E_i electrons in that measurement. This will be a Poisson distribution with $\overline{E_i} = n_e N_i$ and $\sigma_{E_i} = \sqrt{n_e N_i}$. For large numbers the Poisson distribution can be approximated by a Gaussian, so we can write

$$P(E_i|N_i, n_e)$$
$$= \frac{1}{\sigma_{E_i}\sqrt{2\pi}} \exp\left(-\frac{1}{2}\left(\frac{E_i - \overline{E_i}}{\sigma_{E_i}}\right)^2\right)$$

for the ith measurement.

First, we calculate $\overline{E}$, the average number of electrons collected on the CCD.

For σ_E^2 we find

$$
\begin{aligned}
\overline{E} &= \frac{1}{n}\sum_{i=0}^{n-1}\int_0^\infty \mathrm{d}E_i\ E_i\ P(E_i|N_i,n_e) \\
&= \frac{1}{n}\sum_{i=0}^{n-1} n_e N_i \\
&= n_e\overline{N}
\end{aligned}
$$

$$
\begin{aligned}
\sigma_E^2 &= \frac{1}{n-1}\sum_{i=0}^{n-1}(A+B+C) \\
&= \frac{1}{n-1}\sum_{i=0}^{n-1} n_e^2(N_i-\overline{N})^2 + n_e N_i \\
&= n_e^2\underbrace{\sigma_N^2}_{=\overline{N}} + \underbrace{\frac{n}{n-1}}_{\approx 1} n_e N_i \\
&\approx (n_e+n_e^2)\overline{N}
\end{aligned}
$$

In the last step we introduced $\overline{N}$, the average number of absorbed neutrons in a measurement.

and hence

Now we calculate the variance σ_E^2 of the number of collected electrons. To do so, we assume a Poisson distribution for the neutrons absorbed in the measurement. The mean and variance of this distribution will be $\overline{N}$.

$$
\begin{aligned}
r_e &= \frac{\sigma_E}{\overline{E}} \\
&= \frac{1}{\sqrt{\overline{N}}}\sqrt{1+\frac{1}{n_e}} \\
&= r_n\ \sqrt{1+\frac{1}{n_e}}\ .
\end{aligned}
$$

$$
\sigma_E^2 = \frac{1}{n-1}\sum_{i=0}^{n-1} \int_0^\infty \mathrm{d}E_i\ (E_i-\overline{E})^2\ P(E_i|N_i,n_e)
$$

The integral can be calculated in three steps:

$$
\begin{aligned}
A &= \int_0^\infty \mathrm{d}E_i\ E_i^2\ P(E_i|N_i,n_e) \\
&\approx \frac{1}{\sqrt{2\pi n_e N_i}}\int_{-\infty}^\infty \mathrm{d}E_i\ (E_i^2 \\
&\quad\quad -2E_i n_e N_i + n_e^2 N_i^2)\ e^{-\frac{E_i^2}{2\sigma_{E_i}^2}} \\
&= n_e N_i + n_e^2 N_i^2 \\
B &= -2n_e\overline{N}\int_0^\infty \mathrm{d}E_i\ E_i\ P(E_i|N_i,n_e) \\
&= -2n_e^2\overline{N}N_i \\
C &= n_e^2\overline{N}^2\int_0^\infty \mathrm{d}E_i\ P(E_i|N_i,n_e) \\
&= n_e^2\overline{N}^2
\end{aligned}
$$

Bibliography

[Asa03] H. Asano, N. Takenaka, T. Fujii *Flow characteristics of gas-liquid two-phase .ow in plate heat exchanger (Visualization and void fraction measurement by neutron radiography)*, Experimental Thermal and Fluid Science, 2003, in press

[AST] Applied Scintillation Technologies, http://www.appscintech.com

[AST00] Applied Scintillation Technologies, *Phosphor/Scintillator Data Sheet 40*, http://www.appscintech.com/pdf-files/data-sheets/phosphor-data-sheet-40-ndg_iss1.pdf, 2000

[AST01] Applied Scintillation Technologies, *Neutron Glass Scintillators*, http://www.appscintech.com/products/glass-scintillators.html, 2001

[Bal03] M. Balaskó. *private communication*, 2003

[Bal96] V. V. Balashov. *Interaction of Particles and Radiation with Matter*, Springer, 1997

[Bev69] Philip R. Bevington. *Data Reduction and Error Analysis for the Physical Sciences*, McGraw-Hill, 1969

[Bew03] T. Bewer et al. *Novel method for investigation of two-phase flow in liquid feed direct methanol fuel cells using an aqueous H_2O_2 solution*, Journal of Power Sources, 2003, in press

[Bru01] J. Brunner. *Aufbau eines Test-stands für dynamische Neutronen-radiographie eines Verbrennungsmotors*, Diplomarbeit, Technische Universität München, 2003

[Bru02] J. Brunner, E. Lehmann, B. Schillinger, *Dynamic Neutron Radiography of A Combustion Engine*, Proc. 7th World Conference on Neutron Radiography, 2002

[Buc99] M. Buchanan, S. U. Egelhaaf, M. E. Cates. *Dynamics of Interface Instabilities in Nonionic Lamellar Phases*, Langmuir, Vol. 16, 2000, pp. 3718-3726

[Cos01] P. Costamagna. *Transport phenomena in polymeric membrane fuel cells*, Chemical Engineering Science, Vol. 56, 2001, pp. 323-332

[Czi99] J.B. Czirr, G.M. MacGillivray, R.R. MacGillivray, P.J. Seddon. *Performance and characteristics of a new scintillator*, Nuclear Instruments and Methods A, Vol. 424, 1999, pp. 15-19

[Fer02] T. Ferger, H. Abele, J. Brunner, R. Gähler, B. Schillinger, J. R. Villard, *The new station fro fast radiography and tomography at the ILL in Grenoble*, Proc. 7th World Conference on Neutron Radiography, 2002

[Fer03] T. Ferger. *Aufbau einer dynamischen Radiografie- und Tomografiestation mit thermischen Neutronen*, Diplomarbeit, Universität Heidelberg, 2003

[Hub96] J.H. Hubbell, S.M. Seltzer. *Tables of X-Ray Mass Attenuation Coefficients and Mass Energy-Absorption Coefficients from 1 keV to 20 MeV for Elements Z=1 to 92 and 48 Additional Substances of Dosimetric Interest*, http://physics.nist.gov/PhysRef Data/XrayMassCoef/cover.html, 1996

[Hug57] D. J. Hughes. *Neutron Cross Sections*, Pergamon Press, 1957

[IUP01] IUPAC Commission on Atomic Weights and Isotopic Abundances. *Atomic Weights of the Elements 2001*, http://www.chem.qmul.ac.uk/iupac /AtWt/, 2001

[Kak88] A. c. Kak, M. Slaney. *Principles of Computerized Tomographic Imaging*, IEEE Press, 1988, http://www.slaney.org/pct/pct-toc.html

[Kob90] H. Kobayashi, H. Wakao. *Accurate measurement of L, D, and L/D for divergent Collimators*, Neutron Radiography, Proc. 3rd World Conf. on Neutron Radiography, Osaka 1989, printed 1990, pp. 889-892

[Lat62] J. K. Latta. *Water and Building Materials*, Canadian Building Digest, Vol. 30, 1962

[LB90] O. Madelung (editor). *Landolt-Börnstein*, Vol. 11, Springer, 1990

[Leh03] E. Lehmann. *private communication*, 2003

[Mar97] P. D. Marco, W. Grassi. *Overview and prospects of boiling heat transfer studies in microgravity*, International Symposium IN SPACE 97, Tokyo, Japan, November 18-19, 1997

[Mas03] B. Masschaele et al. *Fast neutron radiography and tomography at the ILL*, http://ssf.rug.ac.be/linac/linac /tomography/resultsILL.htm, 2003

[Neu02] Albert-José Dianoux, Gerry Lander (editors). *Neutron Data Booklet*, ILL, 2002

[Nik] http://www.nikon.com

[Ott02] E. Ott. *Einführung in die CCD-Technologie*, PCO-Imaging, http://www.pco.de, 2002

[PCO] http://www.pco.de

[PCO02] PCO, *Bedienungsanleitung SensiCam, Sensicam QE*, Version 02/2002, http://www.pco.de

[Rad17] J. Radon. *Über die Bestimmung von Funktionen durch ihre Integralwerte längs gewisser Mannigfaltigkeiten*, ber. Verh. Sächsische Akad. Wiss., Leipzig, Math. Phys. Kl., Vol. 69, 1917, pp. 262-277

[RIL] *RILEM tube: measurement of water absorption of masonry walls*, http://alcor.concordia.ca/ raojw/crd /essay/essay000285.html

[Rop] http://www.roperscientific.com

[RSI] http://www.rsinc.com/idl

[Sch01] M. Schneider. *Studies for neutron tomography at the Institute Laue-Langevin*, Diplomarbeit Universität Heidelberg, 2001

[Sch99] B. Schillinger. *Neue Entwicklungen zu Radiographie und Tomographie mit thermischen Neutronen und zu deren routinemäßigem Einsatz*, Dissertation, Technische Universität München, 1999, pp. 16-19

[Sea92] Varley F. Sears. *Neutron scattering lengths and cross sections*, Neutron News, Vol. 3, No. 3, 1992. Easy access to data from this article at http://www.ncnr.nist.gov/resources /n-lengths

[SFB01] F. Pischinger (editor). *Abschlussbericht Sonderforschungsbereich 224 (Motorische Verbrennung)*, http://www.vka.rwth-aachen.de/sfb_224/bericht.htm, 2001

[Sie55] K. Siegbahn (editor). *Beta- and Gamma-Ray Spetroscopy*, North-Holland Publ. Comp., Amsterdam 1955

[SIT94] Scientific Imaging Technologies, Inc. *An Introduction to Scientific Imaging Charge-Coupled Devices*, http://astrosun.tn.cornell.edu/courses/astro310/SITe-CCD.pdf, 1994

[Spo69] A.R. Spowart. *Measurement of the absolute scintillation efficiency of granular and glass neutron scintillators*, Nuclear Instruments and Methods, Vol. 75, 1969, pp. 35-42

[Tak99] N. Takenaka et al. *Application of fast neutron radiography to three-dimensional visualization of steady two-phase flow in a rod bundle*, Nuclear Instruments and Methods in Physics Research A, Vol. 424, 1999, pp. 73-76

[Wil02] D. Wildenschild et al. *Using X-ray computed tomography in hydrology: systems, resolutions, and limitations*, Journal of Hydrology, Vol. 267, 2002, pp. 285-297

[YTO] http://www.ytong.com

[Zha99] F. Zhao, M.-C. Lai, D.L. Harrington. *Automotive spark-ignited direct-injection gasoline engines*, Progress in Energy and Combustion Science, Vol. 25, 1999, pp. 437-562

Acknowledgements

Erklärung

Ich versichere, dass ich diese Arbeit selbständig verfasst und keine anderen als die angegebenen Quellen und Hilfsmittel benutzt habe.

Heidelberg, den

Arnd E. Gildemeister

Instructions for the CD

Please find attached to this paper a CD with movies of dynamic radiographies. It can be viewed on any computer that has a Microsoft® PowerPoint® viewer installed. This viewer can be downloaded free of charge from Microsoft's website http://www.microsoft.com. Please open the file **movies.pps** in the viewer. If the movies do not run smoothly, try copying the files to your hard disk and running them from there.